ISSN 2543-9901

JOURNAL OF CASTING & MATERIALS ENGINEERING

AGH UNIVERSITY OF SCIENCE AND TECHNOLOGY
FACULTY OF FOUNDRY ENGINEERING

QUARTERLY
Vol.3 No. 1/2019

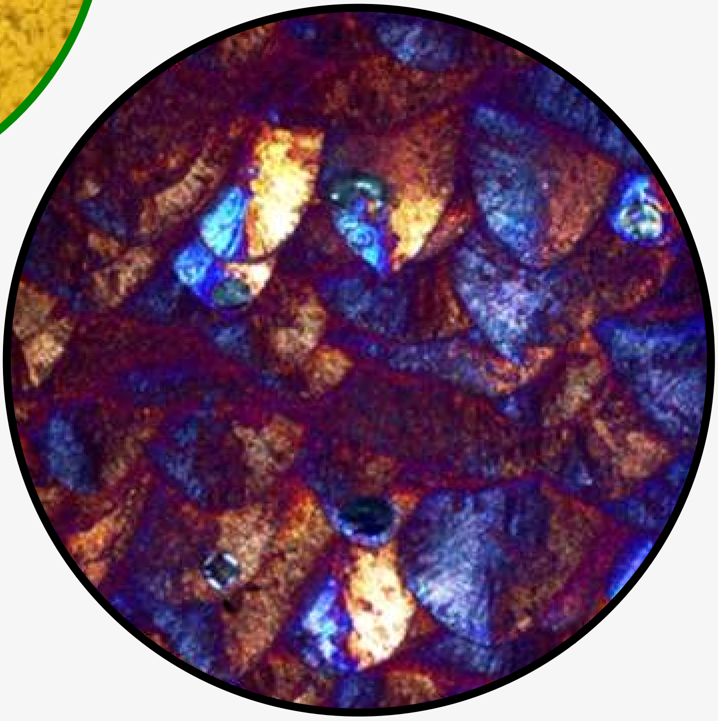

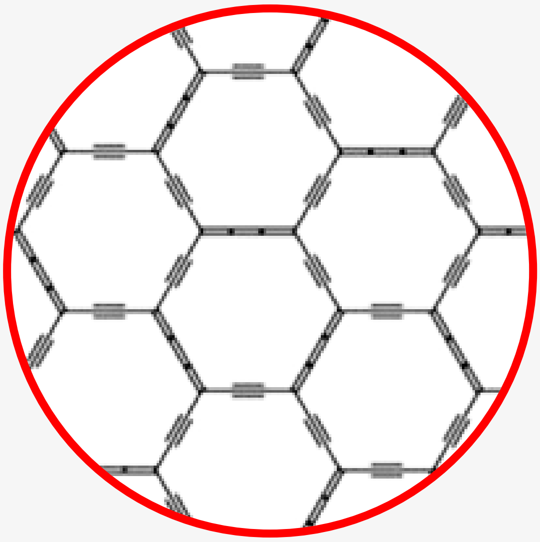

JCME

AGH UNIVERSITY OF SCIENCE AND TECHNOLOGY PRESS KRAKOW 2019

The articles published in the Journal of Casting & Materials Engineering have been given a favorable opinion by the rewievers designated by the Editorial Board.

www:
https://journals.agh.edu.pl/jcme/

AGH UNIVERSITY OF SCIENCE AND TECHNOLOGY PRESS KRAKOW 2019

Wydawnictwa AGH (AGH University of Science and Technology Press)
al. A. Mickiewicza 30, 30-059 Kraków
tel. 12 617 32 28, 12 638 40 38
e-mail: redakcja@wydawnictwoagh.pl
http://www.wydawnictwa.agh.edu.pl

Ministry of Science
and Higher Education
Republic of Poland

Creating English-language versions of publications –
an assignment financed by the Ministry of Science and Higher Education
from resources allocated to science-propagating activities
according to contract 684/P-DUN/2019.

Contents

Journal of Casting & Materials Engineering Vol. 3 No. 1 (2019) 1–13
http://dx.doi.org/10.7494/jcme.2019.3.1.1

Study of AlSi7Mg0.6 Alloy by Selective Laser Melting: Mechanical Properties, Microstructure, Heat Treatment

Arnold Mauduit*, **Hervé Gransac, Pierre Auguste, Sébastien Pillot**

CETIM Centre Val de Loire (CRAI: Centre de Référence de l'Aluminium – pole matériaux et procédés), 3–7 rue Charles de Bange, 18000 Bourges, France
** e-mail: arnold.mauduit@cetimcentrevaldeloire.fr*

Received: 1 February 2019/Accepted: 15 March 2019/Published online: 31 March 2019

Abstract

This study presents a panorama of the AlSi7Mg0.6 (A357) aluminum alloy in additive manufacturing by selective laser melting. The document is mainly interested in the metallurgical tempers obtained after manufacture and after heat treatment; it quickly cover the process. The results concerning the material integrity (porosity), mechanical properties, microstructures, residual stresses, etc., are presented in order to best define the technological capacities of these metallurgical tempers: as-built, soft annealed, T6, and artificial aging. Some information on the mechanisms and kinetics of precipitation is also presented using the Johnson–Mehl–Avrami–Kolmogorov model. Finally, the conclusion proposes an inventory (advantages/disadvantages) of the metallurgical tempers obtained to better understand the industrial applications.

Keywords:

AlSi7Mg0.6 (A357) alloy, selective laser melting, heat treatment (T6, soft annealing, artificial aging)

1. INTRODUCTION

Selective laser melting is an additive manufacturing technique. It is characterized by layer-by-layer construction of a part to be produced: a laser melts the metal powder according to the 3D data entered into a computer. This process is now well-known and documented [1].

The AlSi7Mg0.6 aluminum alloy was historically intended for sand or gravity die casting. Its chemical composition and mechanical properties are specified in the EN 1706: 2010 standard. This alloy is excellent for casting, and it possesses good corrosion resistance, good weldability, and good mechanical properties, which make it a reference for industrial sectors like aeronautics, automotive, and defense. In recent years, this alloy has been used in selective laser melting alongside the AlSi10Mg alloy, which was the first aluminum alloy to be implemented in laser melting. Today, AlSi10Mg is the reference aluminum alloy for selective laser melting [2]. With its silicon content, AlSi7Mg0.6 enables good implementation for laser melting; indeed, it prevents all phenomena of hot cracking that is in the form of interdendritic or intergranular cracking [3]. Several recent studies cover the implementation of AlSi7Mg0.6 (or A357) in laser melting. Most focus is on the powder, on the implementation parameters of the alloy that enable a sound part to be obtained with a minimum of porosity [4], but far fewer documents deal with the microstructure, mechanical properties, heat treatment, etc. Therefore, the study will quickly move on from obtaining and controlling the process parameters to expanding on the metallurgy achieved after laser melting as well as the heat treatment that can be used. Indeed, the main objective of this document is to be interested in the mechanical properties like UTS, YS, residual stresses, the metallurgical structures, and the heat treatment of the AlSi7Mg0.6 alloy resulting from selective laser melting.

2. MATERIALS AND METHODS

2.1. Selective laser melting machine

The machine used for this study is an SLM 280 HL (SLM Solutions) equipped with a 400 W YAG laser. The manufacturing plates are made of an aluminum alloy. The temperature of the manufacturing plate is 150°C. All of the tests were carried out with gas shielding: argon with a minimum purity level of 99.99%. The layer thickness is set to 50 μm, the laser power to 350 W, and the scan speed to 920 mm/s. The manufacturing strategy used is known as "banding," with layers crossed at 90° to the others (the first layer marked with red lines, followed by the second layer marked with green lines). This is shown in Figure 1.

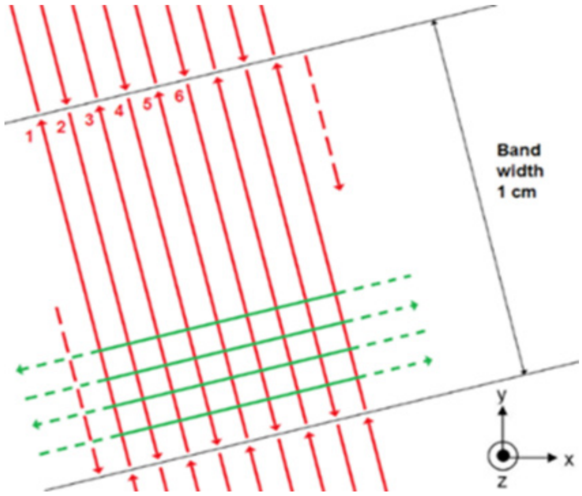

Fig. 1. "Banding" manufacturing strategy

2.2. Powders and test pieces

The AlSi7Mg0.6 powders used in this study for additive manufacturing by selective laser melting are supplied by TLS Technik. Table 1 summarizes the technical data.

The test pieces used for this study are of three types:

- cube: dimension 20×20×15 mm;
- tensile (cylinder with 12-mm diameter and 60-mm length): XY plane or vertical (Z axis) (Fig. 1);
- rod (cylinder with 20-mm diameter and 160-mm length), vertical (Z axis) (Fig. 1).

2.3. Heat treatment

The equipment used for the heat treatment is a forced-air convection oven. This oven is designed for treating aluminum alloys (at temperatures ≤ 650°C) and is characterized by excellent temperature homogeneity (ΔT ≤ 6).

The quenching fluid is cold water (at approx. 20°C). The transfer time of the load (test pieces) in the quenching medium is less than 7 sec in all cases (SAE AMS2772E standard).

The heat treatments performed on the AlSi7Mg0.6 alloy made by laser melting are as follows:

- soft annealed: from 5 min to 2 h at 300°C;
- artificial aging: from 5 min to 24 h at 170°C;
- T6 temper (solution heat treatment + quenching + artificial aging): 2 h at 540°C + water quenching + 6 h at 170°C.

2.4. Characterization tests

Porosity

Porosity measurements use the Archimedes or three weighings method [2, 5]. This is the method most often used for quickly determining the porosity of parts and test pieces made through additive manufacturing (selective laser melting). Porosity measurements by image analysis are also used on the cube test pieces. These measurements are made with an optical microscope – an Axio Imager M2m (Zeiss).

Hardness

Brinell hardness measurements are performed at room temperature with an Emco Duramin 500 test machine (EN ISO 6506-1 standard). At least three measurements are performed per test piece (only the average is given).

Tensile tests

Tensile tests are performed in accordance with the ISO 6892-1 standard with a Zwick Z250 tensile machine (250 kN). The test speed is set to 5 mm/min.

Micrographic examination and SEM

Samples for micrographic observation are prepared conventionally (section, coating, polishing, etc.) before observation under an optical microscope – a Zeiss Axio Imager M2m (magnification used from ×50 to ×500).

Table 1
Technical data, powder in AlSi7Mg0.6

Particle size	D_{10} = 11.7 µm D_{50} = 33.4 µm D_{90} = 62.0 µm										
Morphology	Spherical type with some satellites										
Chemical composition		**Si**	**Fe**	**Cu**	**Mn**	**Mg**	**Cr**	**Ni**	**Zn**	**Ti**	**O**
	TLS	6.8	0.17	0.012	<0.005	0.67	<0.005	0.01	0.008	0.18	0.047
	EN 1706	6.5–7.5	<0.19	<0.05	<0.1	0.45–0.7	–	–	<0.07	<0.25	–

Two types of etching were used:

- "sulfuric acid" reagent (10% H_2SO_4, 5% HF, 85% distilled water);
- barker reagent (electrolytic etching).

Samples for scanning electron microscopy (SEM) were observed under an SEM – a Zeiss EVD. This is equipped with an energy dispersive X-ray spectroscopy (EDS) sensor.

Electric conductivity measurement

We use the Foucault currents technique to measure the electric conductivity of non-magnetic metals (which is the case with aluminum alloys).

The instrument used is a Fisherscope MMS pc fitted with an ES40 probe, which is equipped with a thermocouple. The Fisherscope instrument instantly corrects the electric conductivity according to the temperature. We used a frequency of 60 kHz in order to penetrate deep into the alloy.

Residual stress measurements by X-ray diffraction

The measurements consist of collimating a beam of X-rays with the surface of the test piece and measuring the angle of diffraction with which the rays are returned to the detectors (Bragg's law). The angle of diffraction is directly linked to the distance between the atoms of the material. Compressive stress in the same direction as the link between two atoms reduces the interatomic distance; tensile stress increases the interatomic distance. To analyze the stress in one direction, the "sin2ψ" technique described in the EN 15305 standard consists of varying the incident beam angle and in monitoring the change of the angle of diffraction. The measurements were made on an Xstress 3000 G2R instrument.

3. RESULTS AND DISCUSSION

3.1. Preliminary

The manufacturing temperature of the test pieces (manufacturing plate and area) can potentially affect the metallurgical tempers of the AlSi7Mg0.6 alloy. Therefore, three manufacturing temperatures were used: 100, 150 (the temperature mainly used), and 200°C. These temperatures are achievable by the SLM machine: however, temperatures above 200°C are not possible with this device. The other manufacturing parameters remained the same.

The porosity of the test pieces can also affect the mechanical properties, hardness, etc. In order to verify that the porosity level of the test pieces used does not significantly influence the results presented, we measured an average porosity level of 0.67% ±0.20, which remains within the conventional values of additive manufacturing (laser melting).

3.2. Mechanical properties

First, we focused on the mechanical properties obtained with manufacturing at 150°C for the following metallurgical tempers (Fig. 2):

- as-built;
- soft annealed: 2 h at 300°C;
- T6 (solution heat treatment + quenching + artificial aging);
- artificial aging: 2 h at 170°C and 6 h at 170°C.

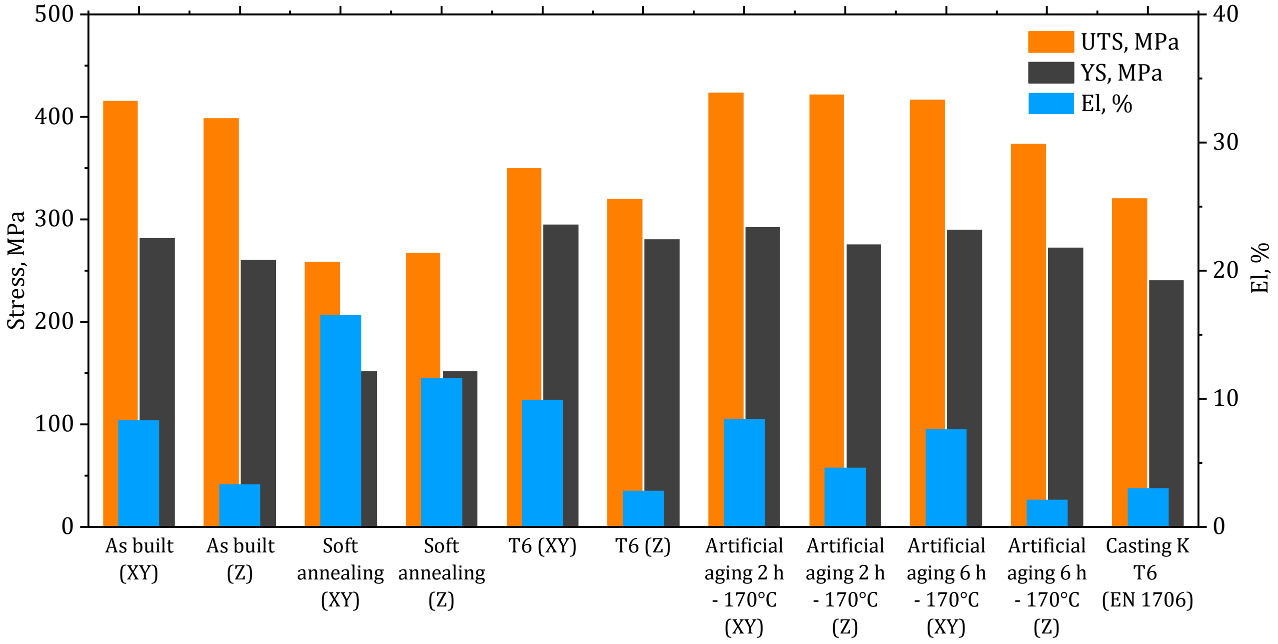

Fig. 2. Mechanical properties (UTS, YS, El) of different metallurgical tempers studied as compared with EN 1706 standard (build at 150°C)

In Figure 2, we note the following:

- The mechanical properties of the as-built, T6, and artificial aging tempers are greater than the minimums of the EN 1706 standard (K T6). Only those that are soft annealed have mechanical properties lower than the standard, which is not surprising.
- The mechanical properties (UTS, YS & El) of the as-built and soft annealed are comparable with the data given in the literature [6].
- The T6 temper normally offers the greatest mechanical properties. In the case of additive manufacturing (laser melting), the T6 temper has a high yield stress, but a marked weakening of the UTS is observed (compared with the as-built temper). Furthermore, the elongation remains limited, especially along the Z axis (barely 3%).
- Artificial aging at 170°C has the most interesting mechanical properties. In this way, 2 h artificial aging at 170°C offers the best compromise in terms of mechanical properties: UTS is the highest of all the heat treatments, and YS remains very close to the maximum obtained with the T6 temper. It can also be noted that the elongation is correct and clearly higher than the minimum of the EN 1706 standard.
- The purpose of soft annealing is to reduce residual stresses. It is clearly noted that it has the weakest UTS and YS, although its elongation is the greatest.
- A certain anisotropy is observed in the mechanical properties on the Z axis (this anisotropy is distinct for elongation).

3.3. As-built

The structures of aluminum alloys (mainly AlSi10Mg) resulting from selective laser melting have been widely studied in the as-built temper [2, 6–9]. The results of these studies are in agreement with the observations made regarding the AlSi7Mg0.6 alloy:

- Highlight the manufacturing strategy: manufacturing tracks are observed on the XY plane and as well as on the Z axis of construction (Figs. 3a–b). In addition, we observe a contour strategy at the test piece's edge (Fig. 3a), which is constituted of three contours: the two outermost are the edge contours (first melted), and the inner one is the filling contour used to join the edge contours and the filling. In Figure 3b (as well as in Fig. 5a and Fig. 10b), the grains in the tracks are oriented perpendicularly to the tangent of the track edges: the grains develop along paths orthogonal to the isotherms in keeping with the laws of solidification.
- Highlight the microstructure: this is constituted of fine dendrites of solid solution aluminum together with Al-Si eutectics (Figs. 3c–d). The observed fine structure can be explained by the extremely rapid cooling of around 10^5 °C/s [2]. Also observed is a coarser structure at the track edge due to the heat reassignment of the area [2].

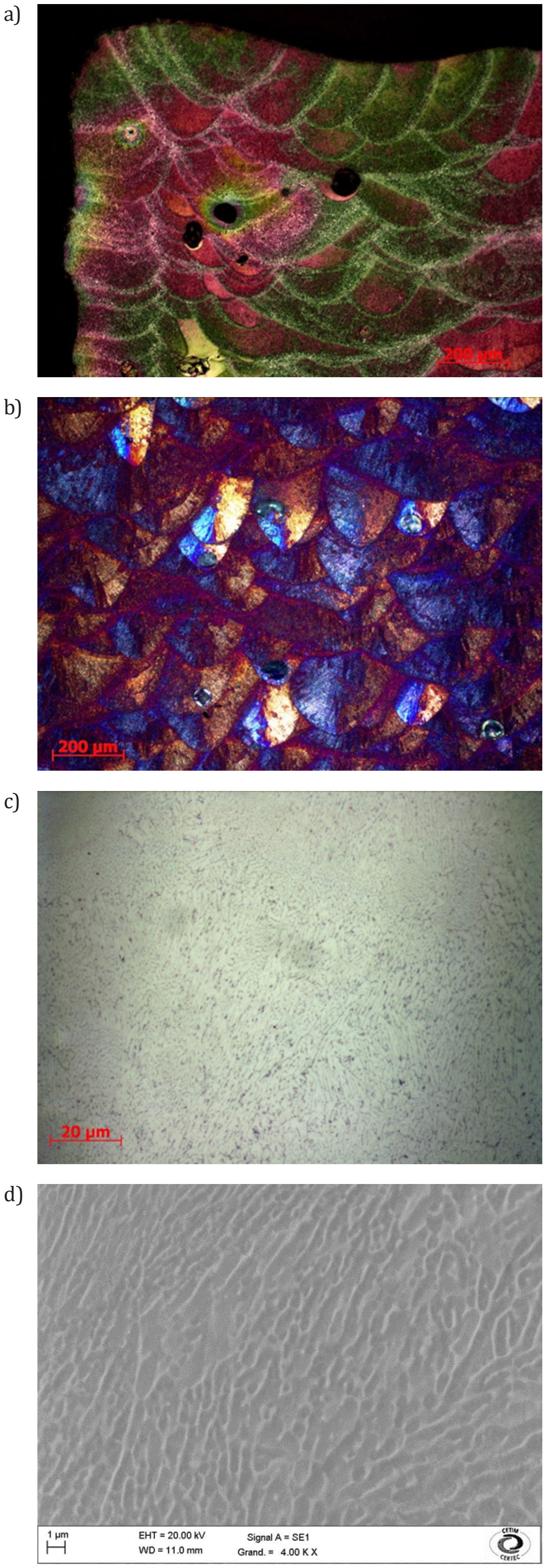

Fig. 3. Micrographic examinations of metallurgical temper studied – As-built: a) and b) strategy of manufacture: beads and grains (optical); c) and d) microstructure (optical and SEM)

In the literature, there is little mention of the fact that the chemical composition of aluminum alloys and, thus, of AlSi7Mg0.6 can evolve after laser melting. However, certain elements making up the alloy in fact evaporate under the effect of high temperatures (for example, magnesium) [3]. In the present case, we see a loss in magnesium of approx. 25% by weight.

3.4. Soft annealing

This treatment is mainly intended for stress relief in order to relax the residual stresses. We created an isotherm at 300°C (from 5 min to 2 h). Figure 4 gives the hardness (HBW 5/250) and electric conductivity results. It can be seen that the hardness decreases with increased treatment time, and the electric conductivity rises. This result is quite standard and perfectly reflects the soft annealing treatment. We note that both hardness and electrical conductivity tend towards an asymptotic limit. The values of hardness and electrical conductivity tend towards those of complete annealing.

The metallurgical structure observed is identical to that of the as-built: manufacturing tracks and the manufacturing strategy can be seen (Fig. 5a). The microstructure is still constituted of fine dendrites of solid solution aluminum together with Al-Si eutectics (Fig. 5b). However, fine dendrites are more difficult to observe and become comparatively “blurred” in the as-built temper (as indicated by [6]).

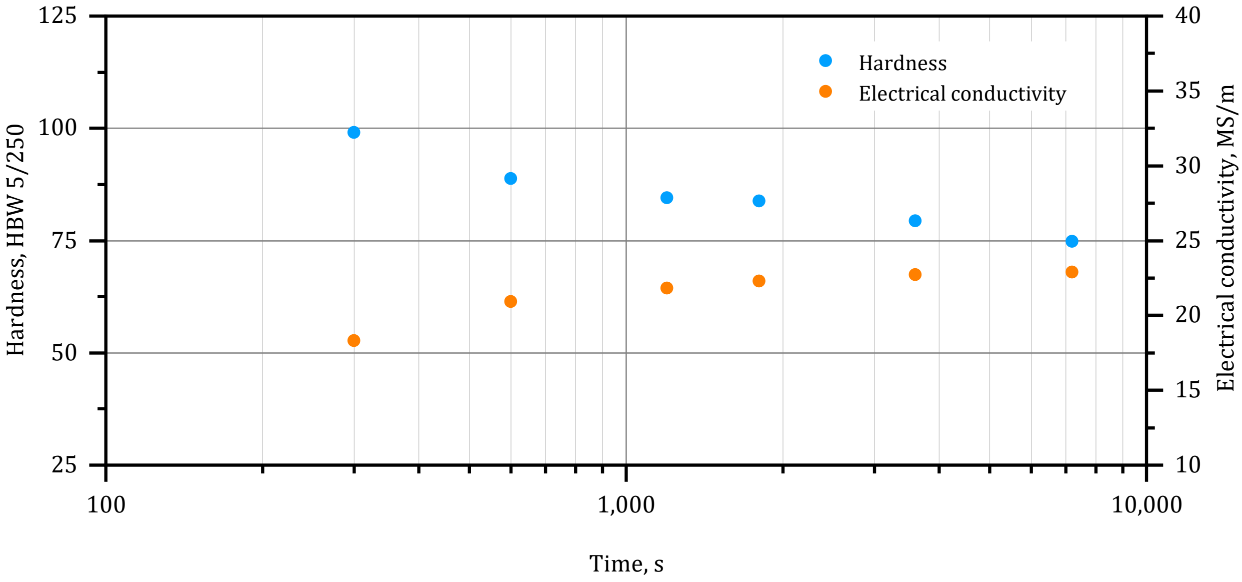

Fig. 4. Change in hardness and electric conductivity according to time of soft annealing

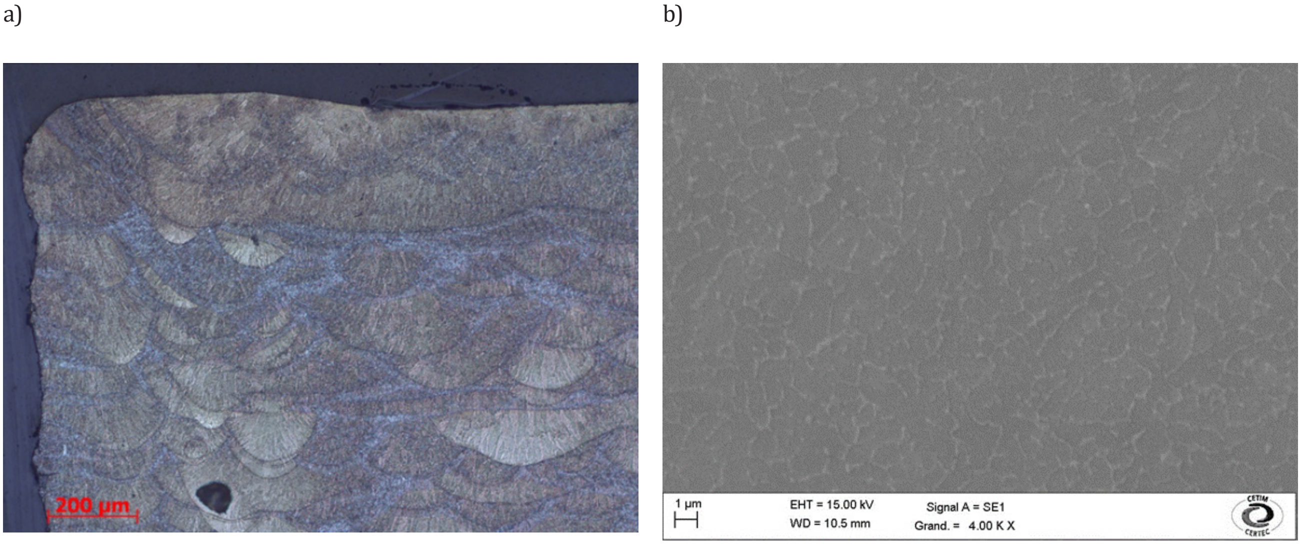

Fig. 5. Micrographic examinations of metallurgical temper studied – soft annealing (S.A.): 2 h at 300°C: a) strategy of manufacture: beads and grains (optical); b) microstructure (optical and SEM)

3.5. T6 temper

The metallurgical structure of the T6 temper is quite different from that of the as-built temper. The manufacturing tracks have disappeared, and the manufacturing strategy can no longer be observed (Fig. 6a). At a higher magnification, Figure 6b shows the structure of the T6 temper, which has changed radically: it is constituted of the aluminum matrix in which small polyhedrons of Si together with fine Al-Fe-Si-type acicular compounds can be observed. Grains (Fig. 6c) that are sometimes underlined by very fine precipitates can just be made out.

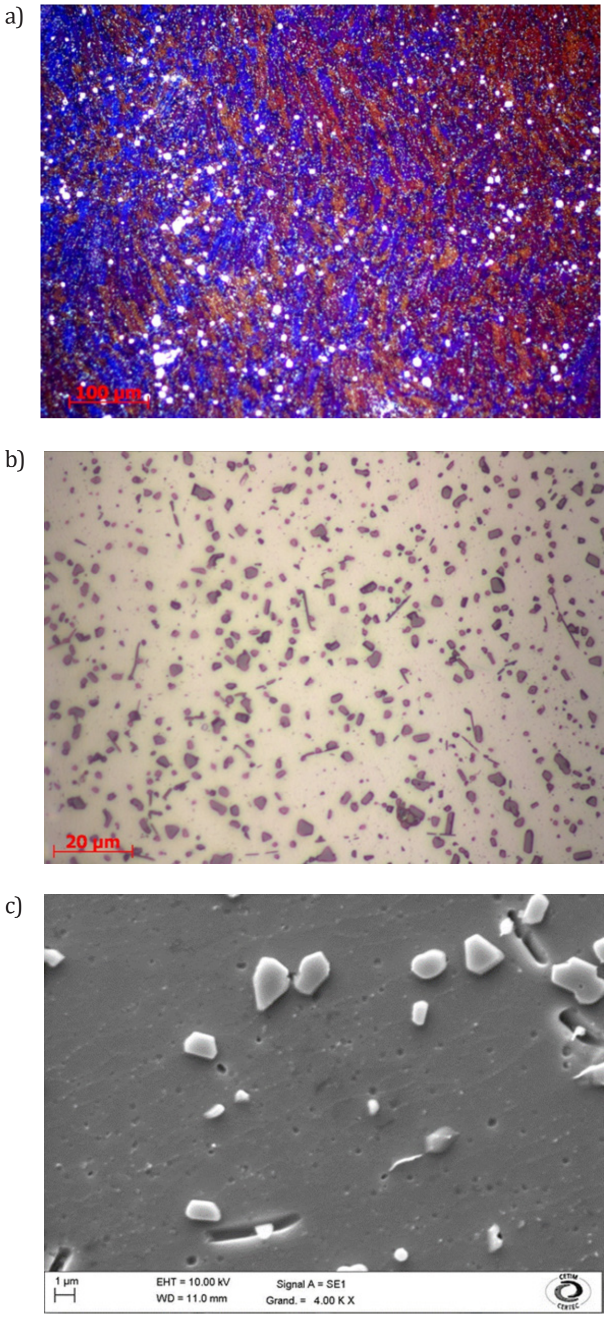

Fig. 6. Micrographic examinations of metallurgical temper studied – T6: a) strategy of manufacture: beads and grains (optical); b) and c) microstructure (optical and SEM)

Rao et al. [10] indicate that the possible origin of the silicon polyhedrons is due to an oversaturation of the solid solution aluminum in the silicon in the as-built temper; this is likely related to the rapid cooling. Thus, the solubility of silicon in the solid solution aluminum exceeds 1.6% by weight (this value is nevertheless the maximum limit of the solubility in the aluminum at the eutectic temperature), eventually reaching values of approx. 5% by weight. During the solution heat treatment, the oversaturated solid solution aluminum breaks down, and the solubility of the silicon "naturally" falls below 1.6% by weight by forming the silicon polyhedrons visible in the T6 (as well as the T4) temper.

Another phenomenon appeared during the solution's heat treatment (2 h at 540°C): the porosity level increased. An increase in the number and size of porosities were seen after the solution heat treatment. This phenomenon is shown outwardly by the appearance of blisters on the surface of the test pieces (Fig. 7). Figure 7 clearly shows a difference in the quantity and size of the porosities before and after the solution heat treatment. The porosity level measured on a micrographic section on the same test piece indicates an increase in porosity; in the as-built temper, the level is 0.43% – after the solution heat treatment, the level rose to 1.01%.

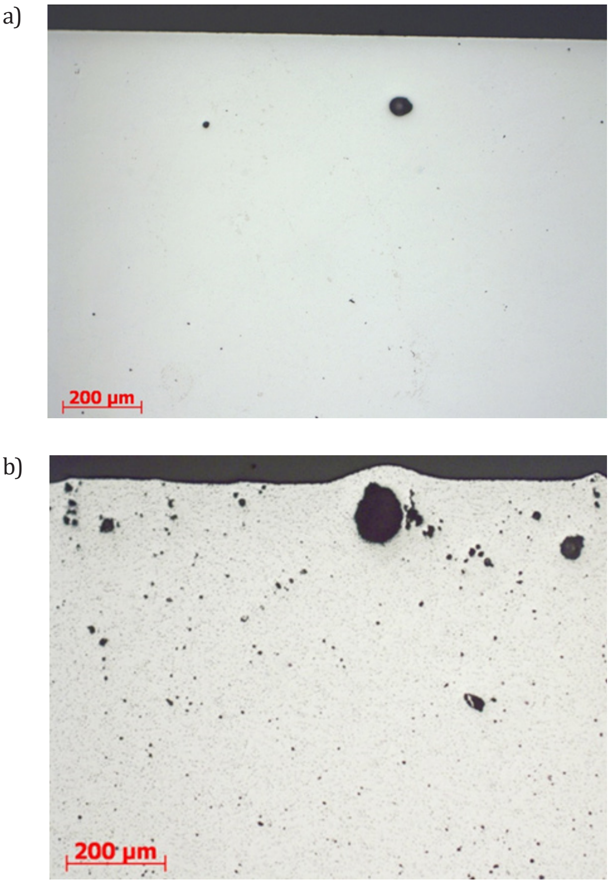

Fig. 7. Change in porosities before and after solution heat treatment: a) as built; b) T6

In Figure 8, the number of fine porosities after solution treatment "explodes" as compared to the as-built: there are more porosities, and they are larger. These are attributed to the trapped gases (hydrogen) in the molten pool during solidification [11]. During the solution heat treatment, the hydrogen migrates, forming more new porosities (and larger ones at that). This conclusion seems to agree with the analyses of Weingarten et al. [12] on the AlSi10Mg alloy.

3.6. Artificial aging (alone) – isotherm at 170°C

On the as-built temper (with manufacturing carried out at 100, 150, and 200°C), an artificial aging treatment (6 h at 170°C) was performed. The mechanical properties obtained are given in Figure 9. There is a decrease in UTS and YS with the manufacturing temperature along with a slight rise in elongation. This can be explained by the fact that the build carried out at 200°C passed to over-aging with the treatment of 6 h at 170°C. The artificial aging of 6 h at 170°C has the most impact in terms of UTS and YS on the build at 100°C, which is explained by the fact that the temperature at 100°C has no influence on precipitation: the hardening potential is not initiated, and the best mechanical properties are obtained. The build at 150°C has good mechanical properties that are slightly weaker than the build at 100°C. This can be explained in the same way as above: the test pieces passed to slight over-aging.

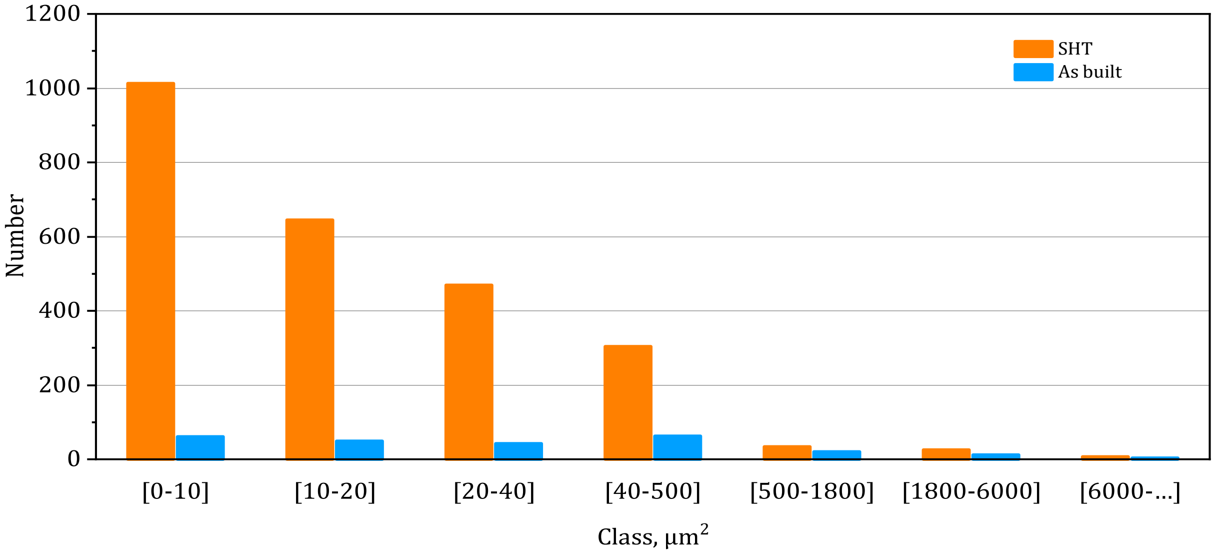

Fig. 8. Distribution of porosities in as-built temper and after solution heat treatment

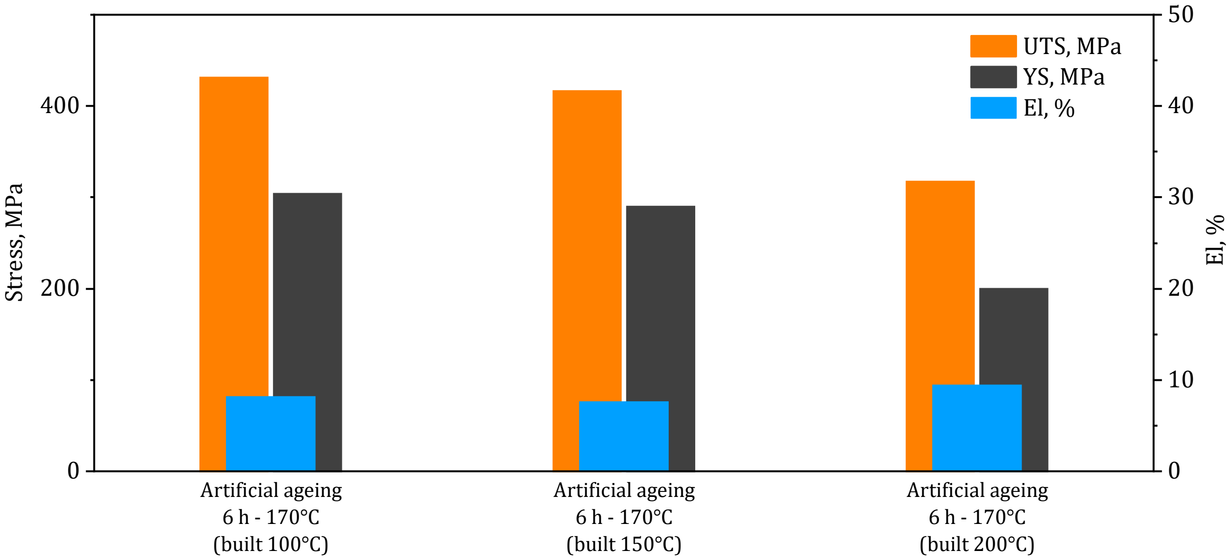

Fig. 9. Conventional mechanical properties (UTS, YS, El) after artificial aging 6 h at 170°C on three builds (at 100, 150, and 200°C)

The metallurgical structure of the test pieces after artificial aging for 6 h at 170°C (Fig. 10a–c) has not changed when compared with the as-built temper and are comparable to the builds at 100, 150, and 200°C.

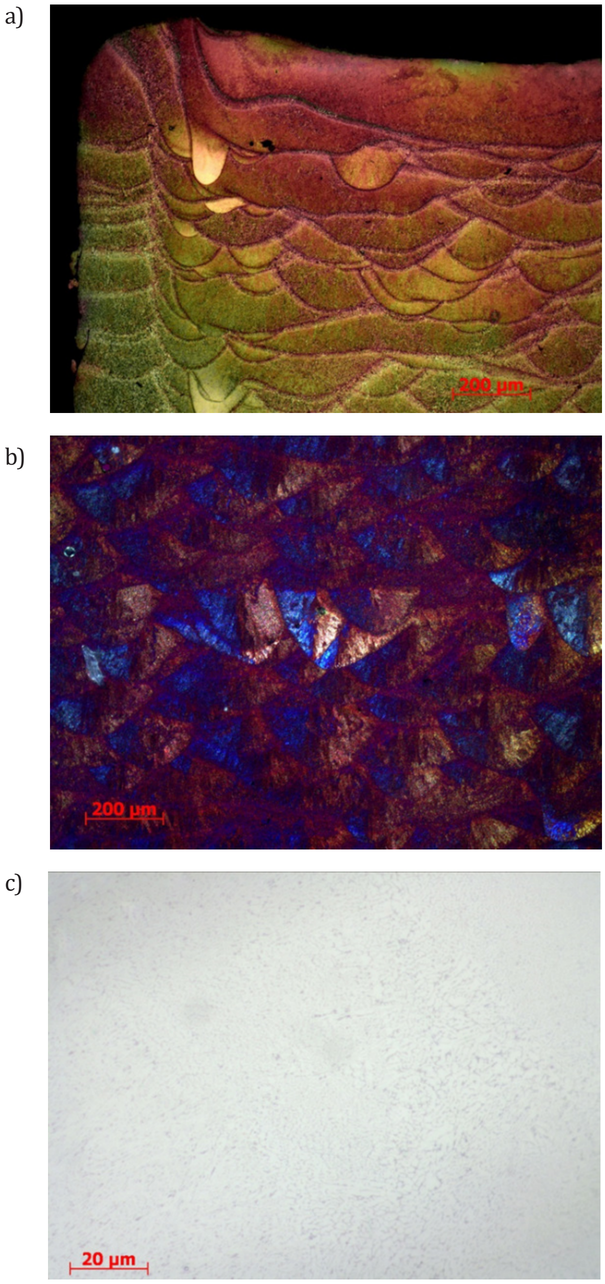

Fig. 10. Micrographic examinations of metallurgical temper studied – artificial aging 6 h – 170°C: a) strategy of manufacture: beads and grains (optical); b) and c) microstructure (optical and SEM)

On the as-built temper at 150°C, an isotherm at 170°C was created (5 min to 24 h). Figure 11 shows the change in electric conductivity and hardness according to the exposure time to 170°C. It can be seen that the electric conductivity increases and hardness reaches a peak at approximately 3 h of exposure. Thus, the maximum mechanical properties would be reached in artificial aging at approx. 3 h.

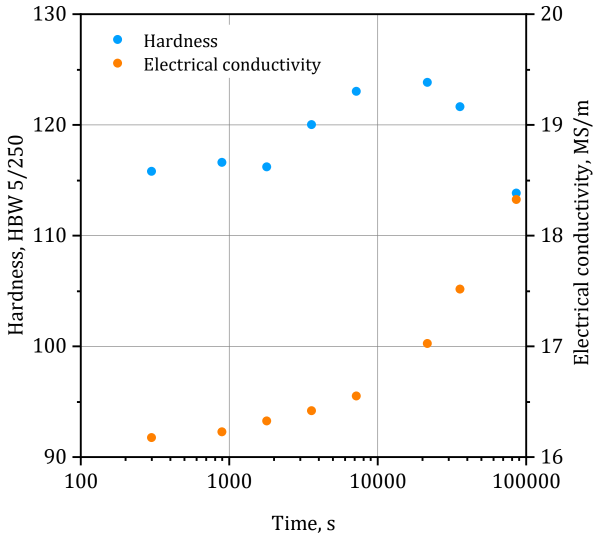

Fig. 11. Changes in hardness and electric conductivity according to artificial aging time at 170°C

Among the experimental methods to study the structural precipitation of aluminum alloys are macroscopic physical methods; these use macroscopic variations of an alloy's physical properties (electrical, thermal, dimensional, etc.) according to its state of precipitation. Electric conductivity (and conversely electric resistivity) are governed by the state of the breakdown of the solid solution of the aluminum alloy studied [13].

The isothermal transformation kinetics that proceed by germination and growth are often described by the Johnson–Mehl–Avrami–Kolmogorov (JMAK) model, which assumes random germination and uniform growth. The JMAK model is based on the concept of "extended volume," which is the volume that a new nucleus would occupy in the absence of the encroachment or overlapping of an already transformed adjacent nucleus [14].

$$x(t) = 1 - \exp(-[k(T)t]^n) \text{ (JMAK model)} \tag{1}$$

where:

$x(t)$ – the transformed volume fraction;
n – called the Avrami exponent, which is an indication of the transformation mechanism;
t – the isothermal hold time;
$k(T)$ – a speed constant essentially dependent on the temperature.

And so $k(T)$ can be expressed by an Arrhenius equation:

$$k(T) = k_0 \exp(-\frac{E_a}{RT}) \tag{2}$$

where:

E_a – the activation energy for isothermal germination and growth;
k_0 – a constant.

As shown above, the electric conductivity is governed by the state of the breakdown of the solid solution (of the aluminum alloys) and, thus by the transformation kinetics (precipitation and dissolution of the precipitates).

Thus, the volume fraction $x(t)$ transformed in an isothermal reaction can be described as follows:

$$x(t)=\frac{\sigma(t)-\sigma_0}{\sigma_f-\sigma_0} \tag{3}$$

where:

- $x(t)$ – volume fraction transformed in time t (isothermal transformation;
- $\sigma(t)$ – electric conductivity in time t;
- σ_0 – initial electric conductivity;
- σ_f – final electric conductivity.

The JMAK model can be applied to the previous results.

The volume fraction transformed in time t: $x(t)$ can be obtained from the measurements of electric conductivity given above. Then, it is possible to determine the parameters of the JMAK model from the previous equations as follows:

$$\log\left(\ln\left(\frac{1}{1-x(t)}\right)\right)=n\log(t)+n\log(k(T)) \tag{4}$$

then, it is a matter of plotting $\left(\ln\left(\frac{1}{1-x(t)}\right)\right)$ according to $\log(t)$. If the model applies, a straight line should be obtained (possibly one straight line per portion). In this case, n (the Avrami exponent) is the slope of the straight line, and $n\log(k(T))$ is the ordinate at the origin. We obtain n and $k(T)$ (Fig. 12); thus, $n = 1.19$ and $k(T) = 3.2310^4$. As shown previously n, is called the Avrami exponent, which supplies an indication of the transformation mechanism. Here n, is close to 1, so it involves needle thickening [15]. According to the literature [16], we have precipitation of the phase β'' (as fine needles), then β' (as needles then rods), and finally β as plates or laths. Thus, the value of n(close to 1) can transcribe the precipitation of β'' and β' as far as needle thickening, which can be similar to rods. This is confirmed by Figure 11, where peak hardness (and thus the peak of the mechanical properties) is obtained by the precipitation of β'' and β'.

3.7. Build height

We measured the hardness on cylindrical test pieces with a height of 160 mm. These test pieces were manufactured at 100, 150, and 200°C. We compared the results obtained (Fig. 13). It should be recalled that the rapid cooling (around 10^5 °C/s) during manufacture causes a quench effect on the test pieces.

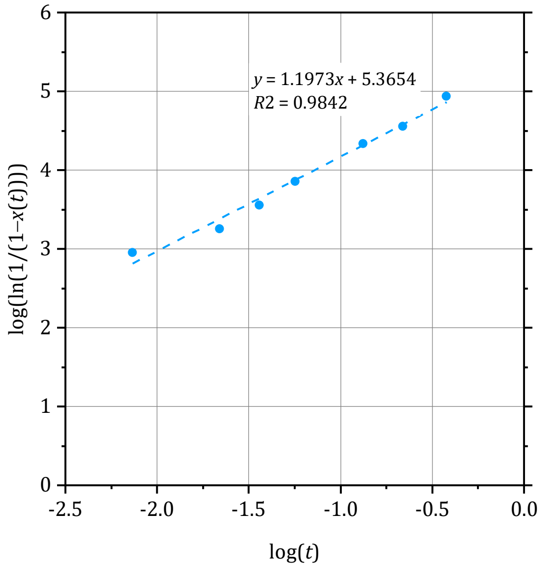

Fig. 12. Application of JMAK model on electric conductivity

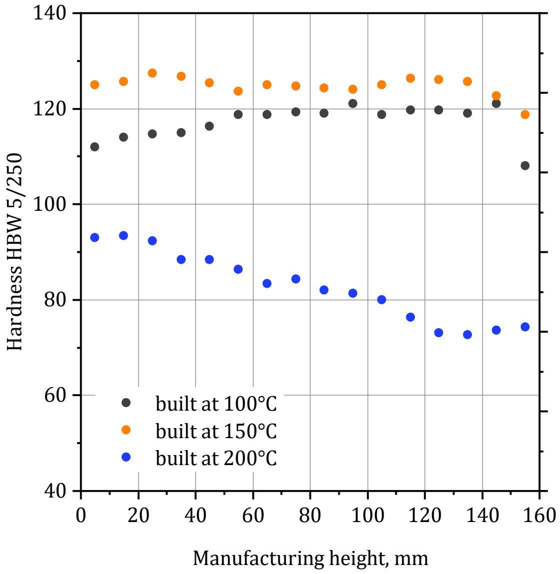

Fig. 13. Hardness tests carried out on height of test pieces manufactured at 100, 150, and 200°C

Figure 13 leads us to these reflections:

- The build at 200°C has the lowest hardness because the manufacturing temperature at 200°C necessarily means the mechanical properties are reduced by the over-aging effect (the standard artificial aging for this alloy is 6 h at 170°C). The reduction in hardness with build height can have several origins: a lower cooling speed (hence, a coarser structure) and greater difficulty to evacuate heat on the powder-bed (hence, a higher manufacturing temperature, which means greater over-aging).

- The slight increase in hardness for the build at 100°C (approx. 112 to 121 HBW 5/250) is explained in the same way as above; i.e., it is undoubtedly harder for the heat to be evacuated, which increases the manufacturing temperature with the build height. Thus, the start of artificial aging appears (under-aging). The final drop in hardness is explained by a temper close to maturation (T4 temper).
- For the build at 150°C, the stability of the hardness values can also be explained by this effect of the temperature increase with the build height. Artificial aging (certainly longer for lower builds) is carried out at 150°C (manufacturing temperature), and the artificial aging for the higher builds (certainly shorter) is carried out at higher temperatures (a rise in temperatures with the height of the build).

On these same as-built test pieces, we applied different heat treatments:

- solution heat treatment + quenching + artificial aging: T6 temper,
- artificial aging (6 h at 170°C).

We then proceeded with new hardness measurements that we compared with the as-built value and found the following (Fig. 14):

- the T6 temper enables the hardness values to stabilize over the whole build height, and the same hardness to be obtained whatever the manufacturing temperature;
- artificial aging (6 h at 170°C) enables the hardness values to stabilize for the builds made at 100° and 150°C; this is explained by the fact that the manufacturing temperatures are below the artificial aging temperature and that a precipitation potential remains (which is not the case for 200°C).

3.8. Residual stresses

Residual stresses are internal stresses present at equilibrium in a mechanical part. The state of the residual stresses in the part is the result of the entire manufacturing scheme (the processes). During the manufacture of the part, uncontrolled relaxation of the residual stresses can cause detrimental deformations. After being put into service, any residual stresses present at the end of manufacturing are added to the external mechanical stresses. As a result, they affect the part's lifetime. In general, residual compression stresses at the surface are beneficial and cause an increase of resistance to fatigue or to corrosion under stress. Tensile residual stresses are penalizing and correspond to areas at risk of premature failure.

The test pieces used for the study of residual stresses are cylinders with a diameter of 12 mm and length of 60 mm (attached or detached from the manufacturing plate).

The studied test pieces in the AlSi7Mg0.6 aluminum alloy are given below:

- as-built attached to the plate and detached from the plate;
- solution heat treatment (2 h at 540°C) + quenching (in water) + artificial aging (6 h at 170°C) attached to the plate and detached from the plate;
- artificial aging (6 h at 170°C) attached to the plate and detached from the plate.

The measurements are taken as follows in the same way on each test piece (Fig. 15):

- one area in the middle of the test piece;
- one area 7 mm from the end: edge (1 or 2);
- one end area (1 or 2).

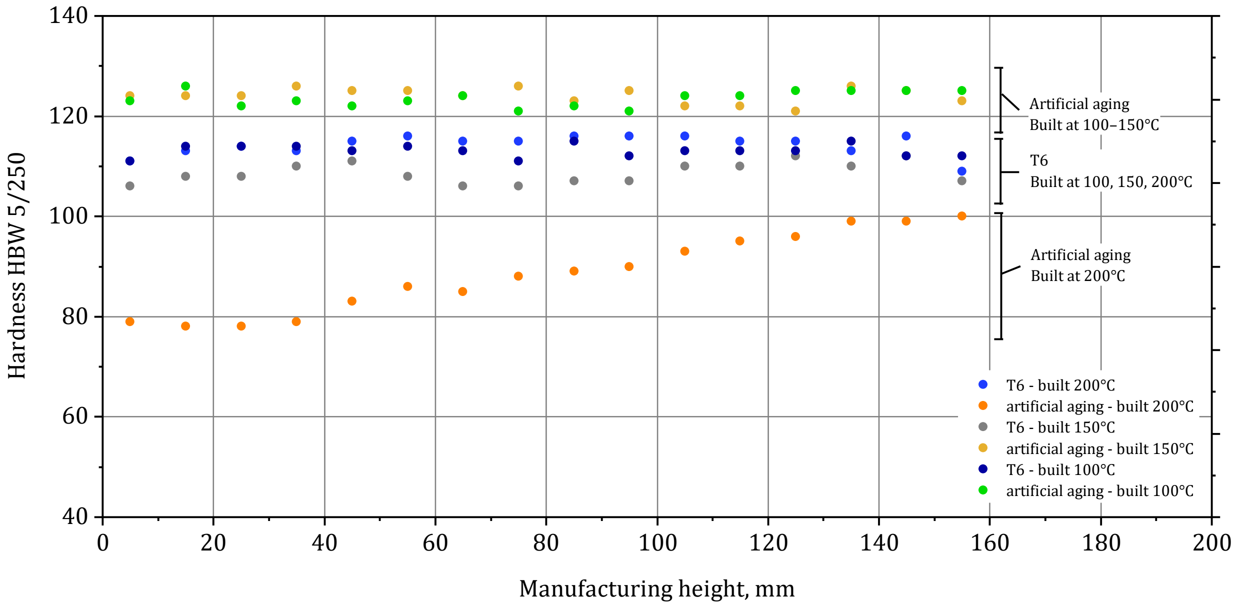

Fig. 14. Change in hardness with build height (100, 150, and 200°C) according to heat treatment (T6 and artificial aging)

Fig. 15. Illustration of measurement areas and directions analyzed

For each area, the residual stresses are measured (Fig. 15):

- at 850 μm deep;
- in the axial and crosswise directions for the "edge" and "middle" areas;
- in Directions 1 and 2 for the "end" areas.

Note that the measurement uncertainty is estimated at ±3% for the depths as well as for residual stresses at ±30 MPa.

The "as-built attached to the plate" test piece has the greatest residual stresses – between 120 and 160 MPa (as per area) – except for the end in Direction 2, where the stresses are weaker (at around 25 MPa). The greatest stresses are obtained at the edge (Fig. 16).

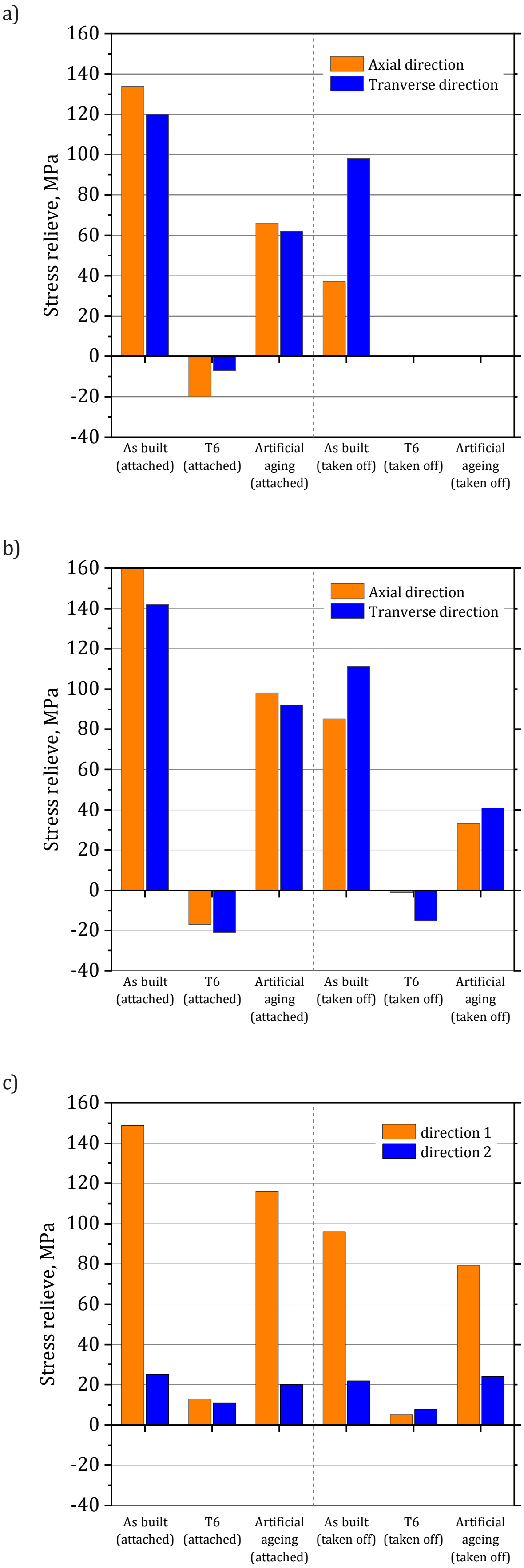

Fig. 16. Change in residual stresses according to measurement location, heat treatment, and whether or not test piece was attached to manufacturing plate: a) middle; b) edge; c) end

The "as-built detached from the plate" test piece has weaker residual stresses than the previous test piece – these are between 20 and 110 MPa. Note that the greatest stresses are obtained at the edge and the weakest at the end in Direction 2. Compared with the "as-built attached to the plate" test piece, the stresses reduced by approx. 30 to 75 MPa. Also note that, in the crosswise directions, the stresses are less relaxed by cutting and not at all in the case of Direction 2 (Fig. 16).

The "T6 attached to the plate" test piece has the weakest stresses and sometimes in slight compression (between 10 and -25 MPa). The same test piece detached from the plate shows an almost identical profile. Note that the residual stresses measured in the different areas are more homogeneous (tighter values). The test pieces from this temper have the weakest tensile residual stresses (Fig. 16).

The "artificially aged attached to the plate" test piece has residual stresses weaker than the "as-built attached to the plate" test piece but higher than the "T6 attached to the plate" test piece – these are between 20 and 120 MPa. The measurements carried out after detaching from the plate show a reduction of approx. 50 MPa of the level of residual stresses. Note again that the stresses are less relaxed in the crosswise direction and not at all in Direction 2 (Fig. 16).

It can be seen that:

- The residual stresses are very often highest at the edge and lowest at the end in Direction 2, which seems logical given the shape of the test piece.
- There is a relaxation of the residual stresses of around 50 MPa when the test piece is detached from the plate.
- The more "vigorous" the heat treatment, the more relaxed the stresses. The temper obtained after T6 even has stresses in slight compression.

4. CONCLUSIONS

To demonstrate some originality, the conclusion lists the advantages and disadvantages (seen in this analysis) of the different metallurgical tempers studied previously: this enables a practical link with possible industrial applications (Tab. 2).

Acknowledgments

The authors would like to thank all of the partners of the SUPCHAD (Supply Chain for Aeronautics and Defense) program – Cetim, Safran Electronics & Defense, Zodiac Aerospace, MBDA, ThyssenKrupp, Roxel, Mkair, and Mecabess – for the help provided in carrying out this study.

Table 2
Advantages and disadvantages of different metallurgical tempers studied

Tempers	Advantages	Disadvantages
As-built	▪ No heat treatment; hence, quicker and less expensive. ▪ Useful mechanical properties.	▪ Anisotropy in mechanical properties. ▪ Considerable residual stresses. ▪ Possibility of change in mechanical properties with build's height. ▪ Influence of manufacturing temperature on mechanical properties.
Soft annealing	▪ No (or few) residual stresses. ▪ Isotropic mechanical properties. ▪ More homogenous structure. ▪ No influence of manufacturing temperature.	▪ Weak mechanical properties.
T6	▪ Good mechanical properties: best for YS. ▪ Weak residual stresses (sometimes in compression). ▪ Homogenous structure. ▪ No anisotropy. ▪ No influence of manufacturing temperature on mechanical properties.	▪ Cost of heat treatment. ▪ Increase and enlargement of porosities. ▪ Risk of deformation on quenching.
Artificial aging (6 h at 170°C)	▪ Good mechanical properties: best for UTS – close to T6 temper for YS. ▪ Some facility of heat treatment. ▪ Optimization of artificial aging 3 h at 170°C	▪ Residual stresses. ▪ Anisotropy in mechanical properties. ▪ Influence of manufacturing temperature on mechanical properties.

REFERENCES

[1] Pillot S. (2016). Fusion laser sélective de lit de poudres métalliques. *Technique de l'ingénieur* BM7900.

[2] Mauduit A., Pillot S. & Frascati F. (2015). Application study of AlSi10Mg alloy by selective laser melting: physical and mechanical properties, microstructure, heat treatments and manufacturing of aluminium metallic matrix composite (MMC). *Metallurgical research & technology*, 112, 605. Doi:10.1051/metal/2015039.

[3] Mauduit A., Pillot S. & Gransac H. (2017). Study of the suitability of aluminum alloys for additive manufacturing by laser powder-bed fusion. *U.P.B. Scientific Bulletin series B*, 79(4), 219–238.

[4] Rao H., Giet S., Yang K., Wu X. & Davies C.H.J. (2016). The influence of processing parameters on aluminium alloy A357 manufactured by selective laser melting. *Materials & Design*, 109, 334–346. Doi: 10.1016/j.matdes.2016.07.009.

[5] Spierings A.B., Schneider M. & Eggenberger R. (2011). Comparison of density measurement techniques for additive manufactured metallic parts. *Rapid Prototyping Journal*, 17(5), 380–386. Doi: 10.1108/13552541111156504.

[6] Trevisan F., Calignano F., Lorusso M. & Ambrosio E.P. (2016). Effects of heat treatments on A357 alloy produced by selective laser melting. World PM2016 – Oral session.

[7] Brandl E., Heckenberger U., Holzinger V. & Buchbinder D. (2011). Additive manufactured AlSi10Mg samples using Selective Laser Melting (SLM): Microstructure, high cycle fatigue, and fracture behavior. *Materials & Design*, 34, 159–169. Doi:10.1016/j.matdes.2011.07.067.

[8] Kempen K., Thijs L., Van Humbeeck J. & Kruth J.P. (2012). Mechanical properties of AlSi10Mg produced by selective laser melting. *Physics Procedia,* 39, 439–446.

[9] Manfredi D., Calignano F., Krishnan M., Canali R., Ambrosio E.P. & Atzeni E. (2013). From powders to dense metal parts: characterization of a commercial AlSi10Mg alloy processed through direct metal laser sintering. *Materials*, 6, 856–869. Doi: 10.3390/ma6030856.

[10] Rao J.H., Zhang Y., Fang X., Chen Y., Wu X. & Davies C.H.J. (2017). The origins for the tensile properties of selective laser melted aluminium alloy A357. *Additive Manufacturing*, 17, 113–122. Doi: 10.1016/j.addma.2017.08.007.

[11] Aboulkhair N.T., Everitt N.M., Ashcroft I. & Tuck C. (2014). Reducing porosity in AlSi10Mg parts processed by selective laser melting. *Additive Manufacturing*, 1(4), 77–86. Doi:10.1016/j.addma.2014.08.001.

[12] Weingarten C., Buchbinder D., Pirch N., Meiners W., Wissenbach K. & Poprawe R. (2015). Formation and reduction of hydrogen porosity during selective laser melting of AlSi10Mg. *Journal of Materials Processing Technology*, 221, 112–120. Doi: 101016/j.matprotec.2015.02.013.

[13] Dubost B. & Sainfort P. (1991). Durcissement par précipitation des alliages d'aluminium. *Technique de l'ingénieur* M240v1.

[14] Yan J. (2006). *Strength modelling of Al-Cu-Mg type alloys.* Doctoral Thesis, University of Southampton. Faculty of Engineering Science & Mathematics.

[15] Appolaire B. Croissance/Dissolution, cours théorique de l'INPL.

[16] Fang X., Song M., Li K. & Du Y. (2010). Precipitation sequence of an aged Al-Mg-Si alloy. *Journal of Mining and Metallurgy. Section B: Metallurgy*, 46(2), 171–180. Doi: 10.2298/jmmb1002171f.

Journal of Casting & Materials Engineering Vol. 3 No. 1 (2019) 14–18
http://dx.doi.org/10.7494/jcme.2019.3.1.14

Analysis and Evaluation of Effect of Manganese Content on Properties of EN AC 46000 Aluminum Alloy

Martyna Pasternak*, Marcin Brzeziński, Gabriela Piwowarczyk

AGH University of Science and Technology, Faculty of Foundry Engineering, Reymonta 23, 30-059 Krakow, Poland
**e-mail: martpiw@gmail.com*

Received: 1 March 2019/Accepted: 23 March 2019/Published online: 31 March 2019
This article is published with open access by AGH University of Science and Technology Press

Abstract

This article is the effect of industrial work and many surveys in the one of the Polish foundries that specialize in aluminum alloys. The main goal of our explorations is to evaluate the influence of manganese on Al-Si alloy properties. In die-cast alloys, it is recommended to use larger amounts of iron to reduce the impact on the pressure chamber and mold. Manganese neutralizes the harmful effect of iron by changing the morphology of the separated brittle ferrous phases. The unfavorable form of the iron-containing phases in the form of long needles changes into the forms of fine compact crystals, which are less harmful to the mechanical properties. Nowadays, the main client requirement is to obtain the right parameters at the best price. Specifically, the customer is in the automotive industry, where new technologies provide a connection between the high quality and low weight of car parts [1–3].

Keywords:

aluminum alloy, pressure casting, manganese, strength of material

1. INTRODUCTION

The introduction of a completely new alloy often involves changes in the casting process, purchases of new machinery (or the modernization of the existing devices), training employees, and changes in occupational health and safety conditions. Not only do the casting parameters change, but they are also sometimes further processed. Attention should also be paid to the ratio of the price of alloying elements to the properties obtained by their use. These aspects lead to the correction of existing processes, where sometimes a small change can have great beneficial effects.

The impact of alloying elements are as follows.

- **Copper** – increases tensile strength and hardness as well as improves machinability and resistance to heat loads. At the same time, it reduces elongation and deteriorates corrosion resistance. The change of properties is caused by the strengthening of the α(Al) phase.
- **Zinc** – similar effects as with copper, but its content within a range of 0.05–2% classifies it as an impurity, while it is treated as an alloying element above 5%.
- **Magnesium** – in liquid metal, it combines with silicon to form Mg2Si compounds. These compounds are characterized by variable solubility in the solid solution α(Al), which allows the use of heat treatment in castings made of AlSi alloys. This increases the properties of castings such as their hardness, tensile strengths and yield strengths.
- **Nickel** – has a stronger effect than copper; its effect is noticeable in the case of changes in the mechanical properties of castings operating at elevated temperatures by preventing their deterioration.
- **Silicon** – the basic component of silumins; it has a significant influence on their casting properties. The best results are obtained with the composition of silumins close to eutectic. An increase in its compactness is connected with a decrease in the value of the thermal expansion coefficient of silumens, which is very important in the case of castings operating at elevated temperatures with high requirements for dimensional stability.
- **Iron, tin, lead,** and **zinc** are the main impurities of AlSi alloys, and (as mentioned earlier) Zn can be treated as an alloying element in relevant alloying contents.
- **Iron** in alloys occurs in the form of coniferous crystals of a very brittle Al4Si2Fe compound causing a decrease in mechanical properties, especially the plastic properties and impact strength of castings. The addition of 0.3–0.45% Mn transforms the inclusions of the phase that contains iron into the form of small compact polygonal crystals, which no longer have a negative effect on the strength properties. In die-cast alloys, it is recommended to use larger amounts of iron in order to reduce the effect on the pressure chamber and mold. Higher iron contents therefore require the use of larger amounts of manganese.

- **Manganese** – neutralizes the harmful effect of iron alloy impurities on their mechanical properties by changing the morphology of the separated brittle iron-containing phases. The unfavorable form of iron-containing phases in the form of long needles precipitate into small compact crystals, which are less harmful to mechanical properties. Manganese is also added in amounts of 0.2–0.5% in order to eliminate the negative effects caused by the presence of iron.

Density index – a value used to evaluate the relative content of a casting material. The density of a solidifying casting material is compared at atmospheric and reduced pressures, which is treated as a kind of vacuum. This is expressed by formula (1):

$$\rho_{cast} = \frac{m_{s(atm)}}{m_{s(atm)} - m_{s(water)}} \cdot \rho_{water} \tag{1}$$

where:

$m_{s(atm)}$ – weight of casting material sample determined by method of weighing in ambient air;
$m_{s(water)}$ – weight of casting material sample determined by method of weighing in water;
ρ_{water} – water density at 40°C at pressure of 1013.25 hPa.

Strengthening – the presence of free space in an alloy. This is a casting defect, which is mainly caused by gasification of the alloy in pressure castings. Porosity may have an influence on the decrease of a casting's strength, as the occurrence of porosity causes an increase of the stresses inside the casting, which results in exceeding the yield strength of the material and permanent deformation (which may lead to cracking). There is also the possibility of the so-called notch effect associated with pore geometry. This results in the weakening of the strength of castings at the place of its occurrence.

Shrinkage porosity is caused by a thermo-physical phenomenon consisting of a rapid increase in material volume during solidification. This defect observed on an optical microscope is cave-shaped, as shown in Figure 1.

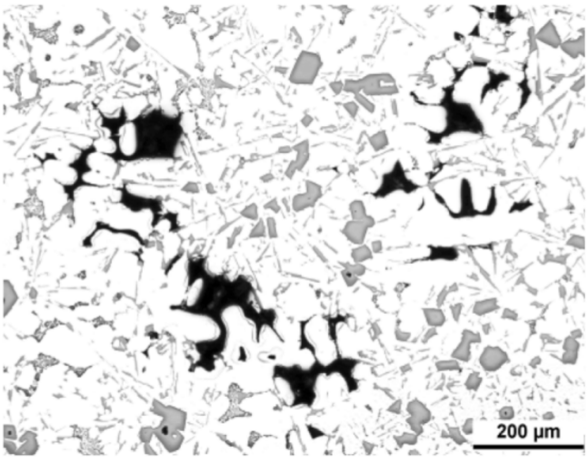

Fig. 1. Shrinkage porosity- microstructural image according to [4]

2. EXPERIMENTAL

The following tests were carried out at a pressure foundry specializing in aluminum alloys. The obtained results refer to the AK 93 alloy (Tab. 1). The high iron content in aluminum alloys, low strength properties of castings, and occurrence of leaks and cracks were the basis for tests on alloys with increased manganese contents.

Due to the need to maintain the continuity of work and to produce many different series of castings at the same time, the following aspects had to be considered:

- no possibility of sudden changes in the chemical composition of an alloy – the necessity of maintaining process continuity;
- compatibility of the metal chemical composition imposed by the standard EN AC-Al Si9Cu3(Fe) [5].

One of the most important parameters is the strengths of material – especially tensile strength. This parameter was the main indicator of the quality improvement related to the increase of manganese content in the aluminum alloy. Additional tests were carried out, such as density index, chemical composition, and X-ray examinations.

Table 1
Chemical composition, % [5]

Alloy	Si	Fe	Cu	Mn	Mg	Cr	Ni	Zn	Ti	Al
Nicromet EN AC 46000	8.71	0.88	2.19	0.471	0.31	0.056	0.045	0.89	0.037	86.3
AK 93 according to EN AC-Al.Si9Cu3(Fe)	8–11	<1.3	2–4	<0.55	0.05–0.55	<0.15	<0.55	<1.2	<0.25	–

X-ray scanning is a good and quick way to show the porosity of a casting. Porosity can effect the strength of castings. This parameter causes an increase in stress inside the casting, which is connected to exceeding the yield point of the material and permanent deformations. In the end, it can lead to a part crack.

Standard EN AC-46000 AC-AlSi9CU3(FE) provides for a maximum manganese content of 0.55% (Tab. 1). Initially, a spectrometric analysis showed a 0.29% manganese content in the alloy, after which it was increased to 0.471% (Tab. 1). The higher content of this element was obtained by adding pigs (bought pieces of alloy) with an increased content of manganese to the alloy. The main problem was the required minimal content (300 kg) of metal in the furnace connected with the die-casting machine. It was not possible to completely empty this furnace and load a new batch; therefore, the chemical composition of the alloy was charged gradually by adding an alloy with a higher manganese content to the furnace. This method was aimed at a slow increase in the content of the element, which is shown in Figure 2. As can be seen, there were large fluctuations in the chemical composition among the successive attempts of the alloy, which is most likely related to the problem of mixing the new alloy introduced into the furnace with the one present earlier.

The increase in Mn content is associated with an increase in production costs, which are at the same time compensated by the smaller number of losses.

Parameters such as the density index, chemical composition, and porosity (X-ray) were examined on several samples with different contents of manganese. The samples were taken during the progressive increase of manganese content in the alloy; the following results refer to the samples with the initial Mn (0.29%) and final Mn (0.47%) contents.

The density index was tested using an MK 300 Electronic Density Index Balance, model MK 3000, harmonized with the EN 55011:2009, EN 55022:2010; EN 61 010-1:2010, EN 61000-6-1:2007, and EN 61000-6-2:2005 standards. The samples were cast into metal bowls and made in two versions: without refining and after refining. Argon was used as a refiner.

The chemical composition was checked using a SpectroMAXx spectrometer with Spark Analyser MX software. The porosity was detected with the use of X-rays. The examination takes place on the basis of the purchased standards, but they are significantly expanded for the needs of the company; each cast detail has its own catalogue of defects and sensitive places to be scanned.

The tensile strength was tested in accordance with the ISO 6892-1 standard [6]. The dimensions of the sample are shown in Figure 3.

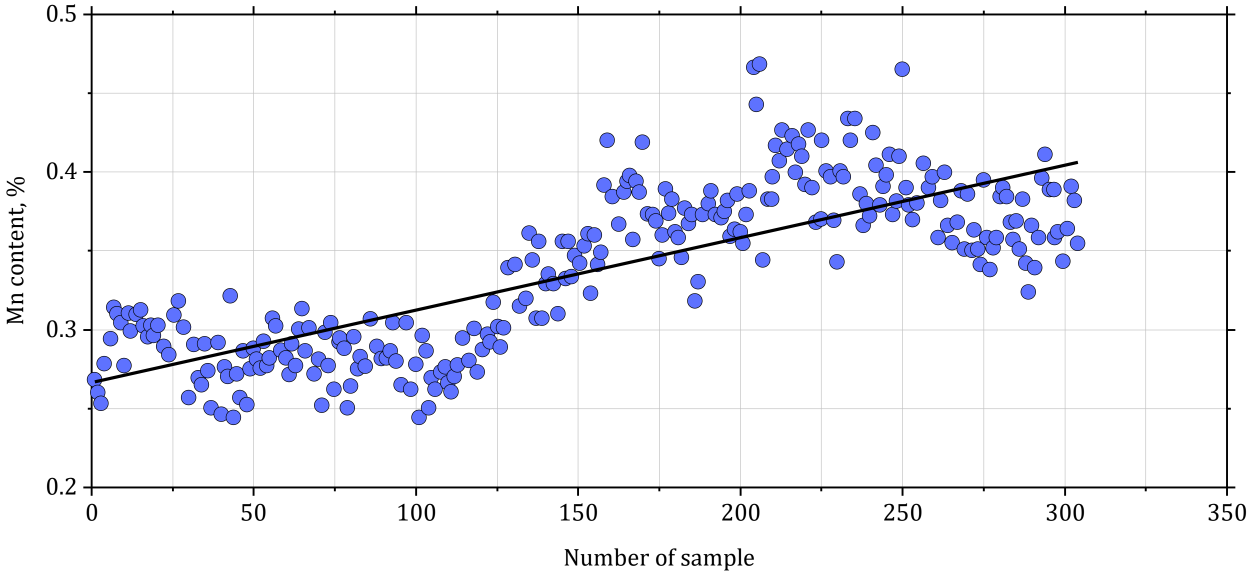

Fig. 2. Course of Mn content growth in subsequent tests of chemical composition

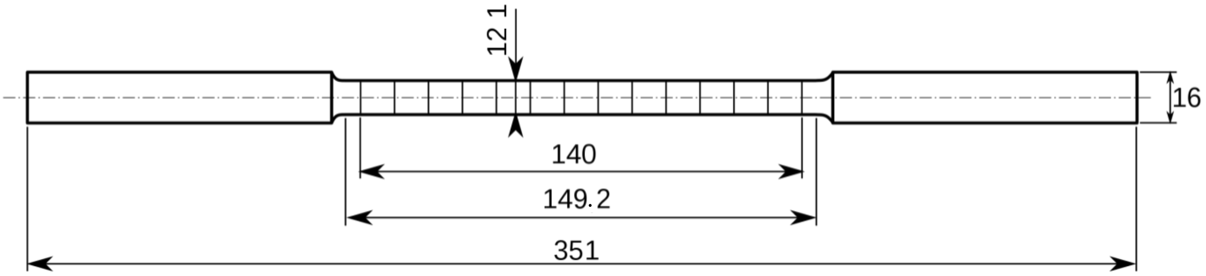

Fig. 3. Dimensions of sample for strength test [6, 7]

3. RESULTS

Conducting research under industrial conditions was a long-term process. The introduced changes could not have a negative impact on the demands placed on the castings; therefore, they had to be done with great attention. As mentioned earlier, changes in the chemical composition of the cast alloy were related to the technological parameters of the casting machine (the minimum metal content of the furnace). During the introduction of new batches of metal into the machine, it was noticed that there are problems with mixing the filled alloy with the alloy that was previously there. Each time, the alloy is subjected to barbotage refining with the use of argon after it has been poured into the ladle and before being placed in a pressure machine.

Example photos of the microstructures for the initial and final contents of Mn in the alloy are shown in Figures 4 and 5. A fragment of an X-ray image is shown in Figure 6. It is a cast image made of an alloy with a high manganese content. The selected fragment is a sensitive area where leakage occurred. Small porosities are acceptable, as this element is impregnated to increase its tightness. In general, it is worth remembering that, in pressure castings, there are always small porosities associated with the specification of this type of casting.

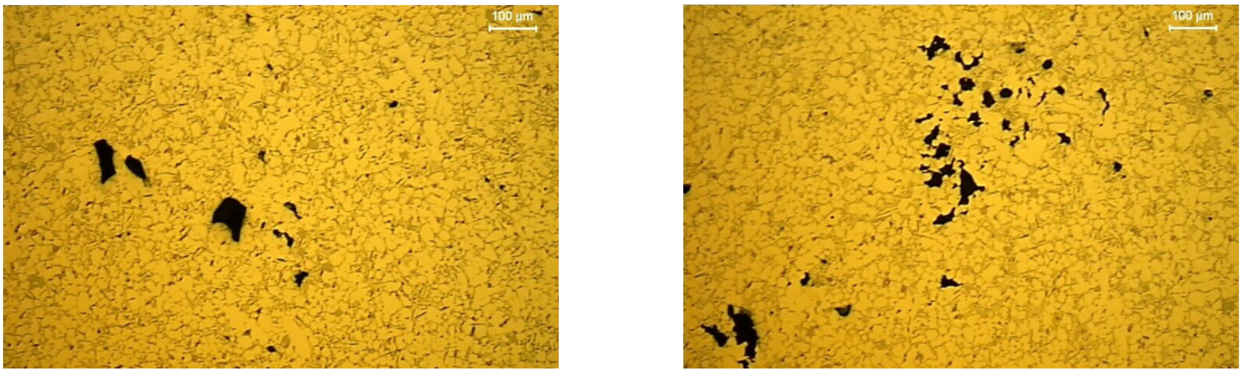

Fig. 4. Microstructure of casting made of alloy with initial Mn content (0.29%)

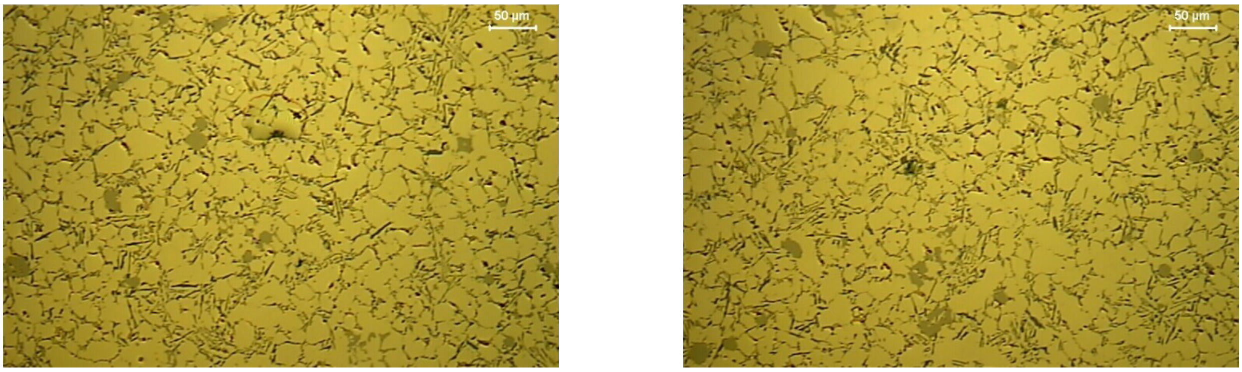

Fig. 5. Microstructure of casting made of alloy with increased Mn content (0.47%)

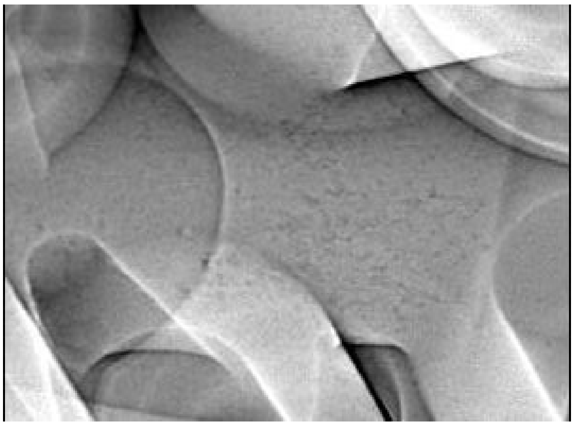

Fig. 6. Fragment of X-ray image

Table 2 compares results of strength test of standard alloy and alloy with increased content of Mn. Table 3 shows the differences in the density index for standard alloy and alloy with increased Mn before and after refining.

Table 2
Strength values

Sample	R_e, MPa		R_m, MPa	
	before refining	after refining	before refining	after refining
Standard alloy	176	185	206.5	214.8
Alloy with increased content of Mn	222	205	231.8	244.5

Table 3
Density index values

Sample	Density index, %	
	before refining	after refining
Standard alloy	6.60	0.64
Alloy with increased content of Mn	3.73	0.54

4. CONCLUSIONS

The obtained results indicated the correctness of our initial hypotheses. It has been discovered that the increase content of manganese affects the following:

- improves strength properties of castings (Tab. 2);
- improves casting microstructures;
- improves density index values (Tab. 3);
- increases tightness of castings;
- stabilizes quality of castings.

The proposed change in production is related only to the input introduced into the melting furnace. The purchase of alloys with increased manganese contents is connected with slightly higher costs, which will be compensated by reducing the shortages.

REFERENCES

[1] Poniewierski Z. (1989). *Krystalizacja, struktura i właściwości siluminów.* Warszawa: Wydawnictwo Naukowo-Techniczne.
[2] Poniewierski Z. (1966). *Modyfikacja siluminów.* Warszawa: Wydawnictwo Naukowo-Techniczne.
[3] Górny Z., Sobczak J. (2005). *Nowoczesne tworzywa odlewnicze na bazie metali nieżelaznych*. Kraków: ZA-PIS.
[4] BDG standard - P202 “Volume Deficits of Casting Made from Aluminium, Magnesium, and Zinc Casting Alloys”
[5] EN AC-46000 AC-AlSi9CU3(FE) (2010)
[6] ISO 6892–1; First edition 2009-08-15
[7] PN-EN ISO 6892-1

Journal of Casting & Materials Engineering Vol. 3 No. 1 (2019) 19–30
http://dx.doi.org/10.7494/jcme.2019.3.1.19

Mechanical and Thermal Properties of Graphene over Composite Materials: A Technical Review

Md. Mashrur Islam[a*], Sadman Saffaf Ahmed[b], Moshiur Rashid[c], Md. Masum Akanda[d]

[a] Department of Electrical & Electronic Engineering, Rajshahi University of Engineering & Technology, Kazla, Rajshahi-6204, Bangladesh
[b] Department of Electronics & Telecommunication Engineering, Rajshahi University of Engineering & Technology, Kazla, Rajshahi-6204, Bangladesh
[c] Department of Mechanical Engineering, Rajshahi University of Engineering & Technology, Kazla, Rajshahi-6204, Bangladesh
[d] Department of Glass & Ceramics Engineering, Rajshahi University of Engineering & Technology, Kazla, Rajshahi-6204, Bangladesh
**e-mail: masumruetgce13@gmail.com*

Received: 25 December 2018/Accepted: 13 March 2019/Published online: 31 March 2019

Abstract

The recent years have seen numerous developments in the research and headway of graphene, the thinnest two-dimensional nuclear material. Graphene-based materials and their composites have promising applications in an extensive variety of fields; for example, gadgets, biomedical guides, films, adaptable wearable sensors, and actuators. The most recent investigations and movement in this branch of knowledge regularly deliver conflicting or uncertain outcomes. This article evaluates and outlines the distributed information in order to give a basic and complete diagram of the cutting edge. Initially, the particular basic nature of accessible graphene materials is illustrated as well as the distinctive generation methods accessible thus far. The appraisal at that point talks about the different composites that center diverse sub-practical routines; for example, mechanical and aggregate utilitarian applications (e.g., vitality, hardware biomedical, layers, and sensors). The use of graphene and its subsidiaries in the fabricate of nanocomposites with various polymer frameworks has been inspected. And finally, an ending and point of view are given to talking about the rest of the difficulties for graphene nanocomposites in useful science and building.

Keywords:

graphene, composite material, modern electronics, sensors, modern materials

1. INTRODUCTION

The fields of nanoscience, nanotechnology, and nanocomposites have developed as of late, and the centrality of this subject growth in the gathering of jobs such as the vehicle, flying, bundling, gadget, biotechnology, adaptable sensor, and different unmistakable applications [1–3]. In such a way, the enhancements of polymer nanocomposites subject to graphene materials have changed into a most imperative advancement. Graphene is a 2D structure of carbon particles that has hexagonal crystalline structure with sp2 bonds, a high surface area (the most raised, adsorption, and surface responses), electron transportability, warm conductivity, and mechanical quality. It has applications in many different fields, including hardware and biomedical [4–8]. It assumes an indispensable job in the upgrade of the relationship between sheets and polymer materials. Graphene-based composite materials are the mainstream for material authorities nowadays, as their crucial improvements result in properties that affect progressively extraordinary applications. In view of its slight physical proximity and helpful electrical, mechanical, and physicochemical properties, graphene is becoming mainstream for the essential vitality fields [9, 10].

In the accompanying areas, we condensed the most recent results in graphene's creation methods (along with its subsidiaries) as well as the properties and development in their composite territory. In the last decade, researches on graphene has been increased expotentially. Those research outputs are very important, this will give us helpful data for the exploration of this zone. The development of this examination area can be obvious from the production record appearing in Figure 1.

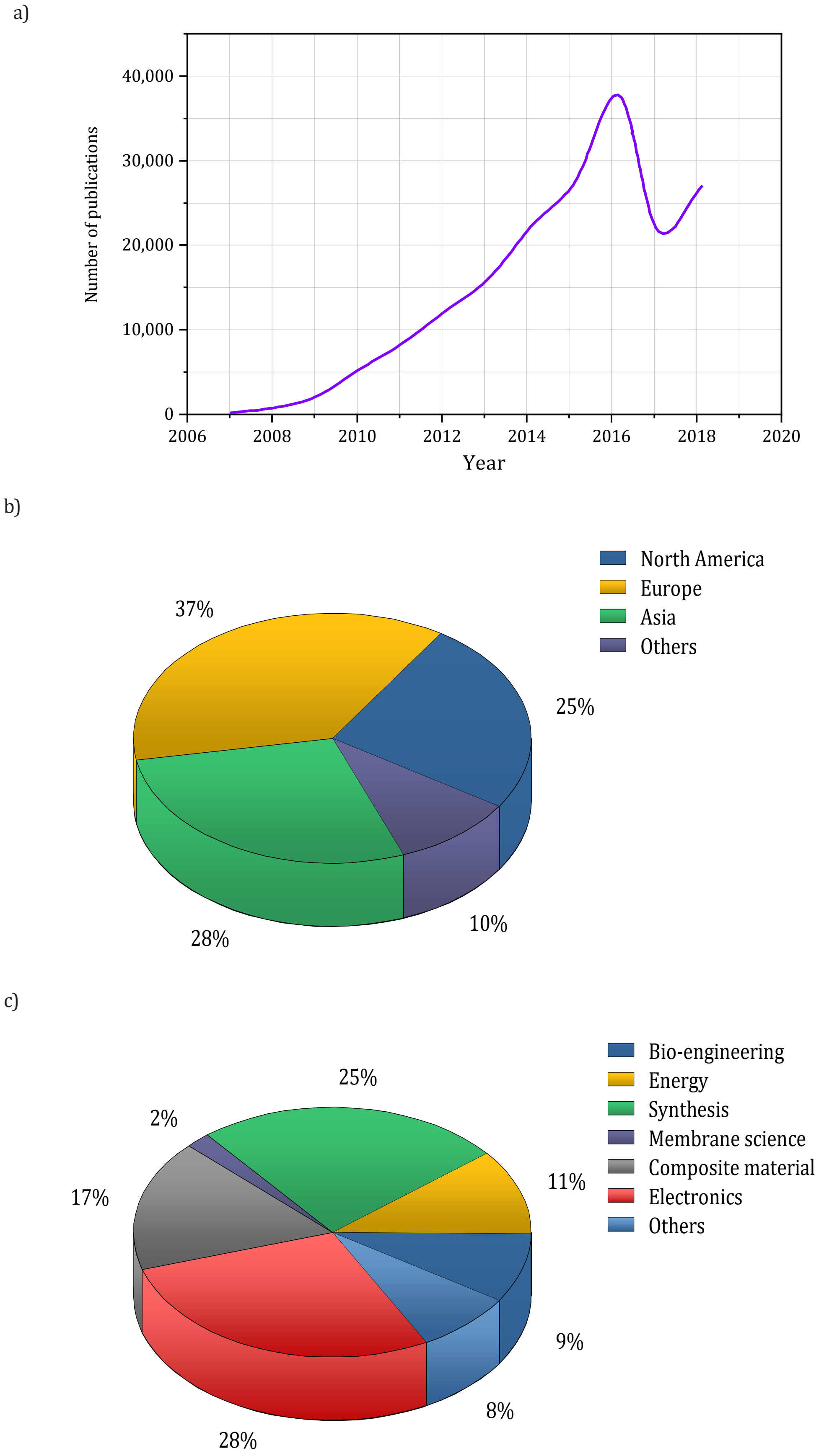

Fig. 1. Researches on graphene in the last decade: a) publications on graphene from 2007 to 2018 (up until August) [Source – SCOPUS & Web of Science], b) proportion of overall publications by countries, and c) by sectors [11]

2. IDEA OF GRAPHENE MATERIALS

Graphene is the slenderest material in its closeness materials. It has a high quantum battle influence, warm conductivity, a high Young's modulus (1 TPa), an unavoidable nature of 130 GPa [12–17], and heat confirmation properties as a solitary sheet. It exhibits the ambipolar electric field influence with section voltage. Graphene is the crucial structure of all other carbon allotropes [18] shown in Figure 2.

It is particularly seen that graphene and its subordinates' potential applications are generally dictated by the unique making of different graphene materials (GO, rGO, fGO, frGO, and mG) with explicit focus on express applications. Those applications are dependent in the chemical behavior of different types of graphene molecular structures. There is an extent of systems and techniques (Fig. 3) that have been advanced. Most of them will be campaigned in the going with region and characterize promising and what's more versatile systems.

Graphene oxide (GO) is unfathomably utilized for composites like fiber-fortified polymer. Carbon fiber and carbon surfaces can be effectively framed by GO to broaden the interfacial holding properties through wrapping the polymer cross areas of the composites. By changing graphene into fiber, the holding limit of the material can be expanded [19–21]. Be that as it may, the framework might be superfluously expensive, as the treatment of each fiber is required. Hung et al. verified the GO outwardly of the surfaces by an electrophoretic sworn articulation method to help the interlaminar shear nature of composites. The technique is humbly basic and quicker. The UTS and Young's modulus of the composites were updated under low-temperature conditions, which is advantage temperature of standard flying machines flying in the troposphere [22, 23].

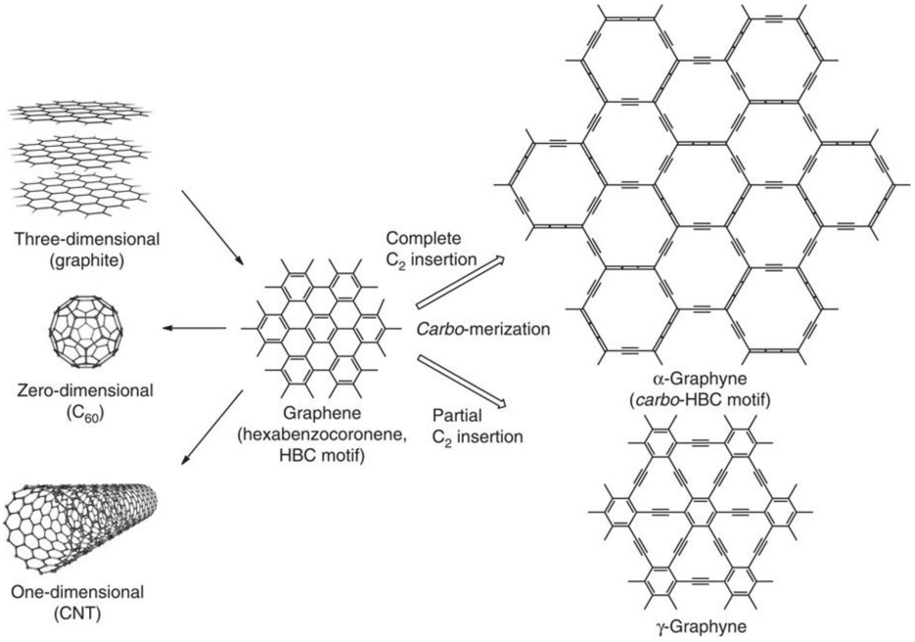

Fig. 2. Chemical structure of graphene material [3–5]

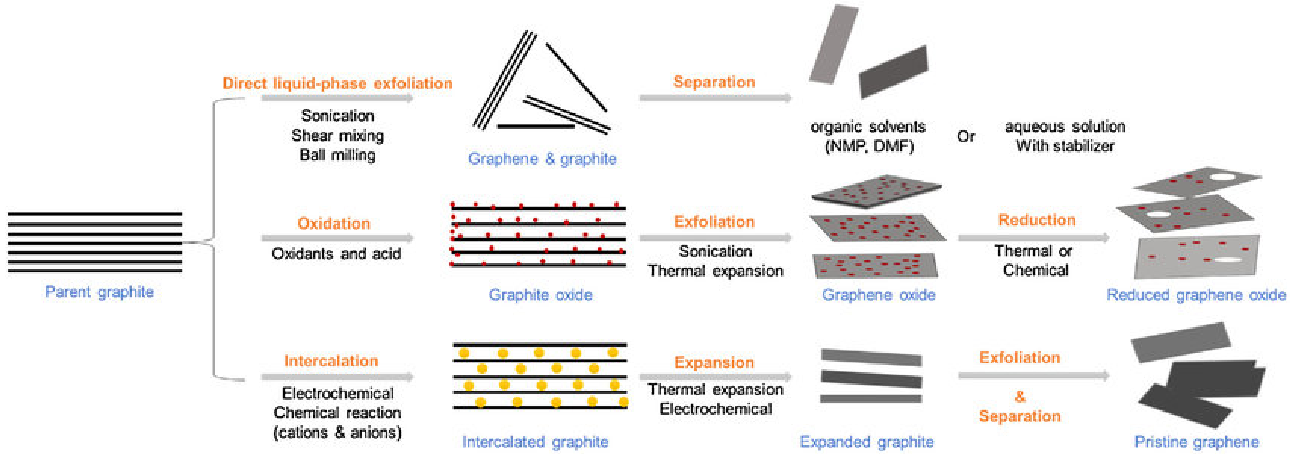

Fig. 3. Production process of graphene material [14–17]

Starting late, GO is used in a like manner as a dielectric material with the true objective of electric insulation along with polarization to special environments. A slender layer of GO film is installed between carbon surface layers, which act as a terminal to outline an essential capacitor. Likewise, GO film can be utilized as a convincing medium to limit essentialness. The range is about 15 to 1500 V. On account of the growing enthusiasm for unmanned air vehicles (UAVs), the imperativeness amassing the cutoff and load of battery reliably limit their flight length to help the power for UAVs, in which the essentialness is achieved from sun-based sheets attached to the outside of the structures [24, 25]. In this structure, UAVs can support imperativeness free from any other individual in the midst of a flight mission.

3. PREPARATION METHODS

A large portion of the exploration contemplates have not utilized graphene in its unadulterated shape (immaculate graphene) because of its restricted yield from the arrangement perspective. Additionally, graphene subordinates (for example, GO, rGO, and frGO) have turned out to be all the more generally accessible and feature comparable properties to those of graphene. The different advances are given below.

3.1. Combination of materials

Little-scale mechanical stripping, mixture vapor dissemination (CVD), liquid stage decline of graphene oxide, and epitaxial advancement are the four assorted built systems for graphene [26]. They are accumulated as a best-down or base-up philosophy. There are different methods to incorporate graphene oxide/graphene, with the quality and measure of the yield depending upon the procedure. Figure 4 demonstrates diverse techniques to design graphene oxide and its subordinates. For this work, the source material will be graphite, oxidized to shed the graphene oxide layer from the mass.

3.2. Liquid stage partition

Graphite oxide was first ever experimentally extracted by Brodie [27] through the oxidation of graphite with potassium chlorate ($KClO_3$) in a graphite and nitric ruinous (HNO_3) blend. This improved the hugeness of the oxidized GO and consolidated the blend course. Regardless, it has wound up being silly because of the drawn-out term of the entire framework to finish; with the advancement of potassium chlorate (and the ensuing chlorine dioxide gas), it was quite perilous. The blend of potassium chlorate and nitric ruinous was recently used to join carbon nanotubes [28] and fullerenes [29]. Incredibly, this oxidation approach showed a lot of oxygen utilitarian parties and discharged dangerous nitrogen dioxide (NO_2) and di-nitrogen tetroxide (N_2O_4). In this manner, the above systems were not exhaustively utilized because of their numbers of restrictions.

3.3. Synthetic vapor affidavit

As contemporary techniques (for instance, little scale mechanical, CVD, and epitaxial improvement approaches to managing yield graphene) have ended up being ordinary, a couple of minor takeoffs from these systems have been developed. The move to move the advancement of graphene on copper foils has recently appeared.

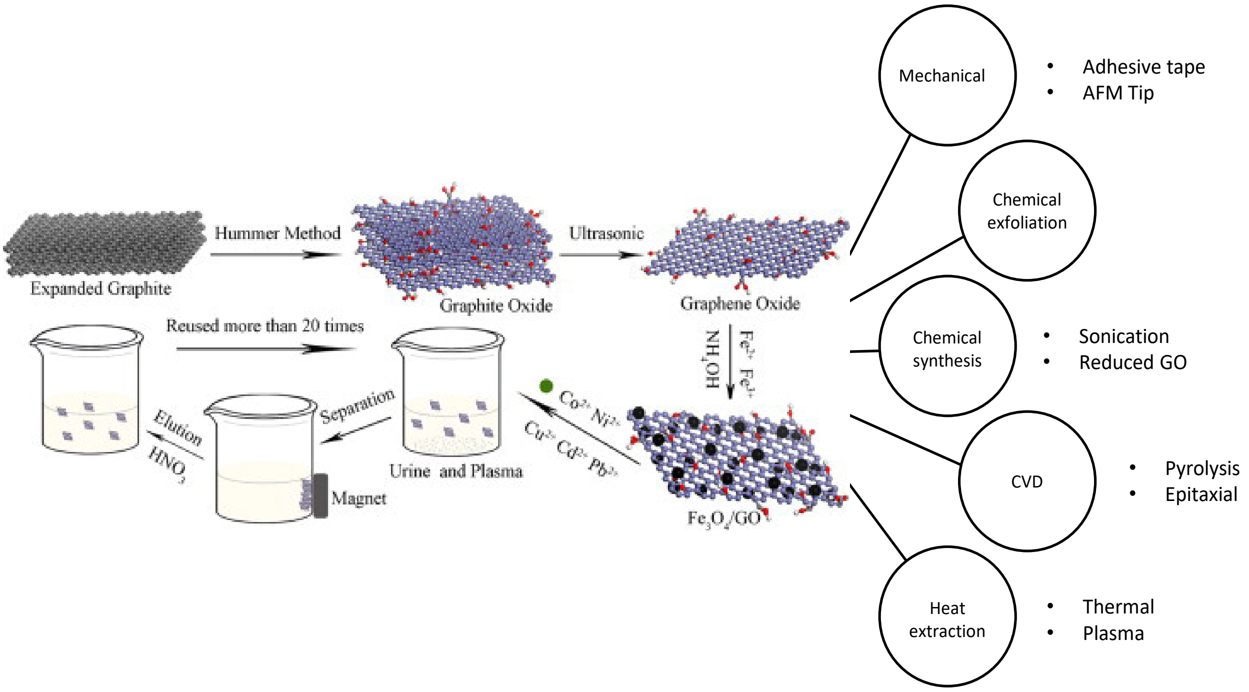

Fig. 4. Methods of extraction of graphene-based oxides. Based on [27]

Additionally, thermally stripped or plasma-helped CVD-made graphene powders could result in the age of CNT on a mass sum, which can be equivalent to the present extensive scale of creation methodologies. The usage of supercritical fluid has central focuses to control the atom gauge and for the uniform spread of nanoparticles all through the composite with zero deformations. Be that as it may, it cannot be used as an alternative in a split second due to the explicit confinements implied by the maker of this examination [30–33].

3.4. Reduction of GO

A reduction results in graphene oxide generally coming back to its special state, which improves its properties (especially its electrical conductivity) [34–42]. This is an objective and imperative development to improve or tailor the properties of GO and perhaps alter the structure of the comparable. There are various sorts of oxide reduction methods of GO shown in Figure 5.

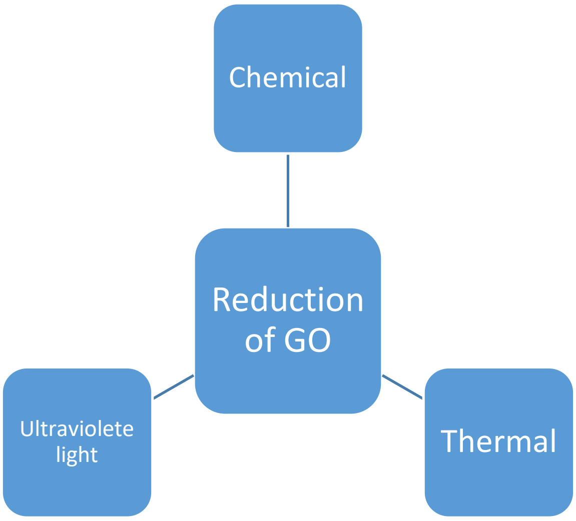

Fig. 5. Reduction methods of GO

Blend decline: Preparation of graphene oxide and decreased graphene oxide in an immense scale, using a convincing and clear strategy [43], wherein GO tests are submerged into a picked engineered lessening master for a particular time allotment and a temperature expanse. This strategy essentially empties the pointless down-to-earth social events (for instance, COOH and OH).

Warm decrease: The warm decay of graphene oxide is more capable of passing on transcendent rGO powders than the vast majority of the materials. In this technique, the GO is reduced at higher temperatures (above or around 1000°C), where the water particles and oxygen reacts very deffusively and is being socked by own [43–49]. UV light decrease: In this strategy, GO is shown to UV light after it is expelled from graphite (either in the suspension shape or the film or powder diagram). On the off chance that the powder GO is to decrease, it will as a rule be scattered in a dissolvable fluid, as the fluid district of GO holds more UV light (making incredibly diminished GO) [50, 51].

Guo et al. [51] electrochemically lessened graphene nanosheets in which GO suspension was done in a three--cathode framework as a power supply and blended for 2 h. Mohan et al. [3] found that the GO decay process is fundamentally time-reliant, as they diminished GO sheets with various decreasing directors for a reaction period up to 100 h. They found that the decay advances as long as three days, which was checked by spectroscopic portrayal philosophies (for example, XPS, Raman spectroscopy, and FTIR) when GO was lessened for up to 50–68 hours.

Most examinations have utilized hydrohalic acids (for example, hydrazine, hydroiodic, hydrobromic, and hydrochloric) to reduce GO [52], which is incited when making rGO with basically less oxygen and carboxylic utilitarian social gatherings. These functionalities are in charge of their last properties, which can be revamped by fluctuating the centralizations of the reducing heads, decay time, and synchronous warming of the blend while diminishing (controlled air). A solid π-π or ionic coordinated effort is made in the wake of purging these supportive parties that enhance the properties. While the GO decay by substance/electrochemical decrease has seen practical decrease portions, the warm decrease of GO is in a like way generally utilized. The quick warming of GO to 1000°C exhausts these utilitarian get-togethers and likely makes incredibly decreased rGO in the edge powders [53, 54]. Obviously, this cannot hold the film kind of GO, which is a negative stamp.

4. MECHANICAL AND UTILITARIAN PROPERTIES OF GRAPHENE MATERIALS

Graphene materials have stable mechanical properties that have future application prospects in the nanoelectromechanical field. The fundamental exact starter examination of the versatile properties and quality of reduced graphene was finished by Lee et al. [55] It was discovered that the graphene exhibits both fragile split and non-arranged versatile leads. Min et al. [56] assessed the shear quality, shear modulus, and split strain of graphene as a part of temperature and chirality through atomic reenactments and announced a break worry of 97.54 GPa and shear nature of 60 GPa when the graphene sheet is exceptionally level. Ovid'ko et al. [57] did experimentation on reduced graphene and had laid down mechanical properties of graphene through test results that ideal graphene has a Young's modulus of 1 TPa and inalienable nature of 130 GPa, which matches the PC reenactments they used for consideration. I.W. Frank et al. [58] revealed that nanometer-thick graphene sheets have a Young's modulus of 0.5 TPa. Neglecting the manner in which that this piece reports conflicting mechanical properties of graphene, it will by and large be comprehended that, when all is said and done, graphene has promising mechanical properties and laudable materials for the further research and application into composite zones. With all of these quality properties, graphene has deserts, for example, openings, grain contacts, and segments that may cause breaks in a rocker or botch point of reference. Thus, it is fundamental to see these flaws better and propose new research thoughts that will decidedly impact the employment of graphene [59–62].

Suk et al. [63] completed a limited-part framework examination on GO. He found that the versatile modulus of flimsy GO ultra-dainty films was reviewed utilizing AFM estimation joined with FEM. GO ultra-meager movies were found to have a Young's modulus of 207.6 ± 23.4 GPa [64, 65] with a thickness kept at 0.7 nm as observed as identical to that of flawless graphene.

The pre-worry of the graphene oxide films was obtained to be 39.78 MPa, which was noted to be one request of a size lower than that of precisely stripped graphene. This story cream system (consolidating AFM and FEM mapping) displayed a course to find the versatile modulus and prestress of slight graphene oxide films. Table 1 plots the latest research centering on the mechanical properties of graphene subordinates.

5. THERMAL PROPERTIES

The warm properties of a material characterize its attributes, while the nuclear structure decides its conductivity. The warm properties of materials change when they are organized on a nanometer scale. The boundlessly substantial inherent warm conductivity of graphene gems has been uncovered from the hypothetical and test thoughts about [69]. The warm conductivity (κ) of a material is specified with respect to warmth motion per unit zone Q″ (e.g., in $W \cdot m^{-2}$) and in contrast to temperature slope $Q'' = -\kappa \nabla T$. The warm conductivity straightforwardly identifies with the explicit warmth by $\kappa \approx \Sigma C v \lambda$, where v and λ are the appropriately arrived at midpoint of the phonon bunch speed and mean freeway, individually [70]. Warm conductivity κ as a component of temperature: the agent information for suspended graphene appears in Figure 6.

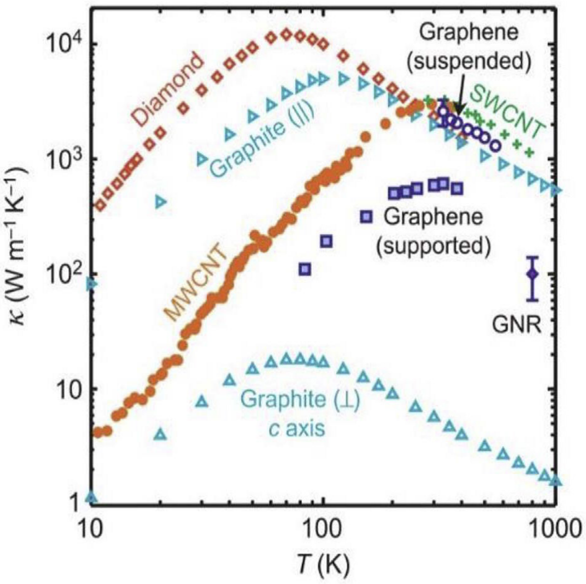

Fig. 6. Thermal conductivity of graphitic materials [70]

6. GRAPHENE-BASED POLYMER COMPOSITES

In this part, we present a sorted-out appraisal of the organization of graphene-based polymer composite distinctive systems, for example, crumble mixing, plan intercalation and atomic estimation scattering of graphene subordinate inside polymer [70–78]. By and large, these sorts of composites have been made utilizing covalently or non-covalently joined systems; for example, in situ polymerization, game-plan mixing/hurling, or dissolve strengthening, or by hybridizing these specific age strategies appropriately.

Based on the properties of the composite material (for example, sub-atomic weight, farthest point, hydrophobicity and open social events), the nanocomposites can be made utilizing these four unquestionable strategies.

Table 1
Survey of mechanical and visual properties of different graphene derivatives

Synthesis Material	Technique of synthesis	Modulus	Shear strength	Young's modulus	Reference
Graphene	Mechanical exfoliation	100–120	60–72	–	[61]
	Molecular dynamics	–	–	1–1.0234	[62]
	Pyrolysis	150	–	0.96	[58]
	Mechanical exfoliation	100	55–85	0.6–0.92	[66]
	Mechanical exfoliation	70–120	–	1.0223	[67, 68]
	Thermal	200–330	30–32	2	[60–66]

The huge scale delivering strategies ought to fulfill the fundamental scale basics for mechanical testing that is either a kilogram of powder or suspension containing graphene chips (routinely of micrometer scale), or a thousand pieces for determined graphene films (generally more noteworthy than millimeter check). The chemical factors needed for converting GO into nano-composites are: (i) the last recommendation to accomplish the properties and packaging/morphology for target graphene things; (ii) the quality and uses of graphene materials; (iii) the adaptability from research office to industry; and (iv) the quality and controllability of storing up, discovering that the vitality age systems utilized in industry are commonly the shedding of graphite, stripping/decrease of graphite oxide, and CVD [79].

Graphene composites can be set up as functionalized nanosheets, fillers, or movies. Additionally, covalent and non-covalent functionalized graphene-based nanosheets were related as 2D models for polymer advancement; the dissolvability is supposedly stretched out with these composites [80].

Graphene-based filler materials have the properties of electrical, warm, and mechanical (which improved it). Be that as it may, layered graphene polymer films are unequivocal for photovoltaic and stack bearing film applications. Chen et al. [81] utilized an atomic-estimation blending technique and started a plasma-sintering procedure to make copper-GNP composites. In the resultant composites, the mechanical execution of the copper that at first upgraded the quality by the advancement of graphene began to incapacitate after a specific estimation. Finally, the break stretching kept diminishing from 30 to 3.5%. Notwithstanding what might be ordinary, the yield quality floods up to 310 MPa at a graphene stacking of 0.6 vol.%; after that, it decays to 200 MPa at 4.0 vol.% of graphene augmentation. The microstructures of the composites appear in Figure 7a.

Fundamentally, Tapasztó et al. [82] understood how to comprehend accomplishing the anisotropic electrical warm and mechanical properties by utilizing shine plasma sintering under uniaxial weight conditions to make GNP-stimulated mud composites (Fig. 7b). Assorted dispersing plans by starting plasma sintering and the perfect introduction of GNPs in the silicon nitride sort out were seen under a microstructural examination.

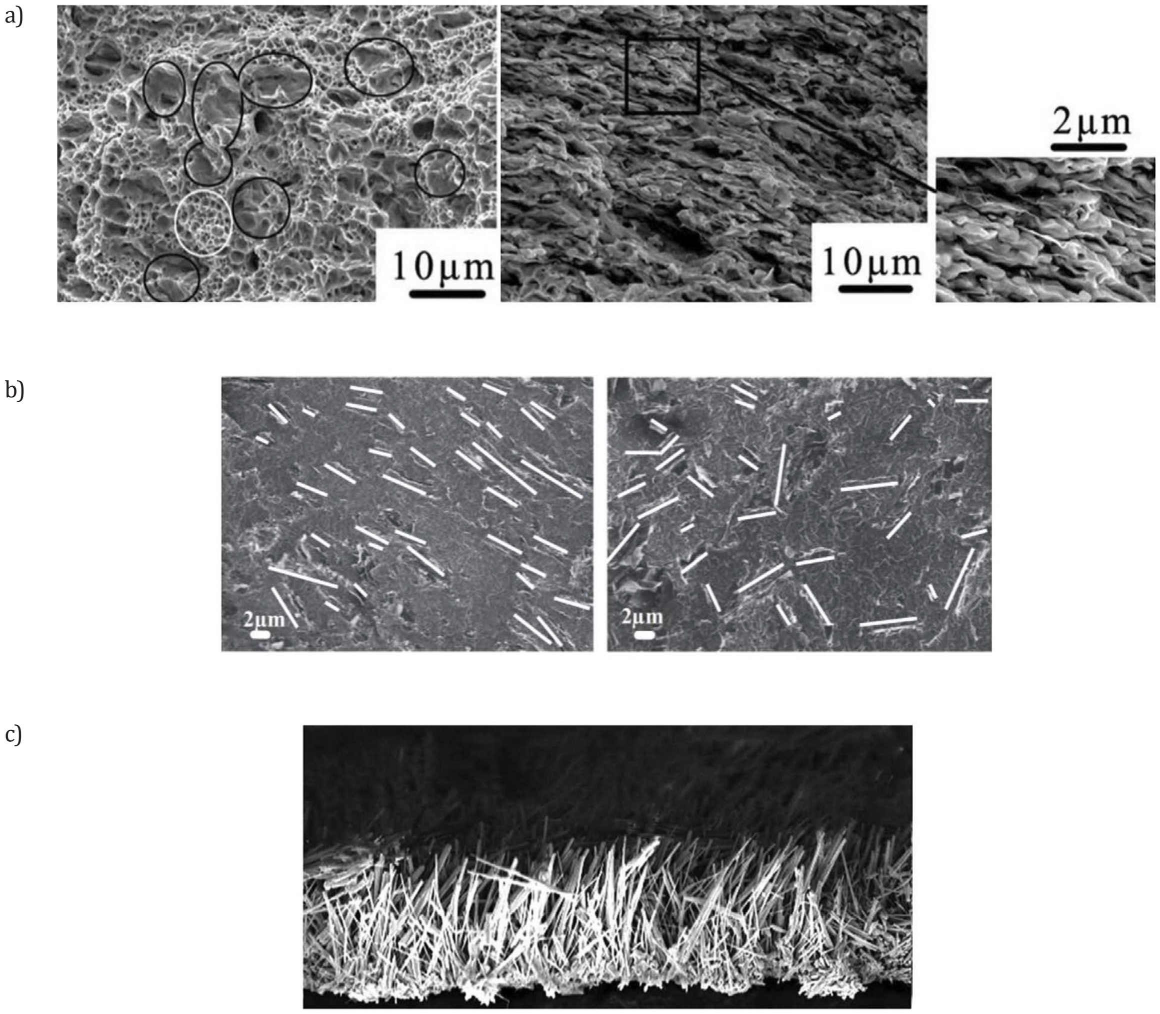

Fig. 7. Micro-chemical analysis using IR imaging: a) spectro images of Cu/GNS composites [78], b) 3 wt.% GNPs in Si3N4 prepared using (left) spark plasma sintering and (right) hot isostatic pressing [81], and c) ZnO2 NWAs/graphene composites [82]

Liu et al. [83] tested the effect of zinc oxide and graphene composite on their optical presentations. The composites were created through a turn covering declaration process as layers of seed ZnO layers being explicitly turned and secured on graphene motion pictures, and ZnO nanowires of around 80 nm were produced hydrothermally from their seeds. This had a higher field enhancement factor of 12,130 with a lower run-on field of 1.74 V/μm as compared to the graphene film layer [84].

The above results exhibit that the comparability of graphene materials in metal lattice composites has been advanced and the dissipating has been cultivated enough using specific techniques; for instance, nuclear measurement mixing and plasma sintering shapes. Zhong et al. [85] orchestrated functionalized diminished graphene oxide (frGO) invigorated styrene butadiene flexible (SBR) for upgraded warm conductivity and developing deterrent. The composites were conveyed from two-miss strengthening sought after by weight forming. The warm conductivity of SBR composites is reliably upgraded with the development of filler content due to the enhanced interfacial correspondence among the frGO and SBR. The warm conductivity was upgraded from 0.15 to 0.38 W/(m·K), and an unbending nature of 22 MPa was cultivated. The developing restriction was extended from 120 h to 240 h, which is twofold the life. This was practiced through amazing dispersing thought the right assurance of functionalizing administrator that manufactures the interfacial bonds between the graphene material and the polymer matrix. The effect of GNP and GO as sustaining pros in high-thickness polyethylene (HDPE) was analyzed by Lin et al. [86] using standard thermo-mechanical blending. In light of the morphological, mechanical similarly as one-of-a-kind physical and thermal property examinations over the ideal polymer graphene, they saw 56% augmentations in the adaptable modulus and 23% development in the most extraordinary weight. The filler loadings were moved from 0.1 to 10% for GNP as well as 0.05 and 1.5% for GO. They saw and assumed that, from their SEM imaging while agglomeration was an issue for the GNP composites at higher weight rates, it was accessible in the GO/MAPE models with loadings as low as 0.25%, attesting that break up blending of GO in HDPE will not result in incredible dissipating.

7. UTILIZATIONS OF GRAPHENE MATERIALS AND THEIR POLYMER COMPOSITES

Because of the likelihood of accomplishing multi-practical properties in polymers by fortifying them with graphene, a few fields have begun utilizing the composites. Fundamentally, there are three primary attributes that characterize the execution of graphene-based polymer nanocomposites:

- nanoscopic detainment of network polymer chains;
- nanoscale inorganic constituents and variety in properties; as revealed by different investigations of their huge change identifying with their size;
- nanoparticle course of action and the making of huge polymer/molecule interfacial region.

Figure 8 presents an alternate field where graphene-based composites are being utilized/inquired about.

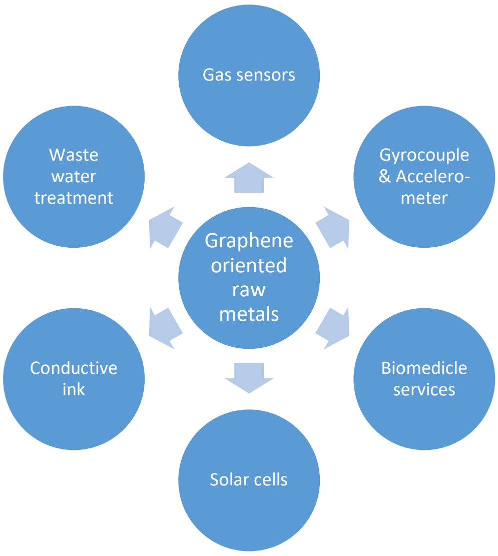

Fig. 8. Key applications of graphene-based composites

7.1. Sensors

The properties of graphene characterize them to be amazingly delicate to the Earth. This affectability expands their sensor application from investigations of the attractive field to DNA sequencing. Speed checking of nearby fluid to strain measures with either electrical or optical insights moderately contends its different applications. A further favorable position of utilizing crystalline graphene is its 20% stretch capacity which increases the analog sensing range of such sensors significantly.

7.2. Vitality and gadgets

Obviously, graphene is a piece of the ongoing quest for an exceptionally equipped sustainable power source. Currently, sun-powered cell advances graphene either goes about as the dynamic medium or as a straightforward/appropriated terminal material. Nonetheless, graphene without a bandgap is probably not going to wind up as a planar channel material in the last decade found in elite coordinated rationale circuits. In any case, numerous other less stringent graphene electronic applications are being set up from the accessible material.

A.I. Fernández-Calvo et al. [87] structured a ultra-capacitor with a particular capacitance of 135 F/g in fluid electrolytes, 99 F/g in natural electrolytes, and 75 F/g in ionic electrolytes [88] separately from a synthetically changed graphene material. These versatile electronic capacity gadgets with high power ability and life cycle are likewise called supercapacitors or electrochemical capacitors. In this investigation by Zhang et al. [89], graphene was blended by mechanical peeling pursued by substance treatment. It is a stretchable anode that can be utilized in different electrolytes and are exceptionally adaptable. For these included properties, supercapacitors can be formulated utilizing a graphene leading polymer composites or graphene change metal oxide composites. A side from utilizing graphene-based metal oxide half and half terminals in supercapacitors for power thickness upgrade, graphene-based batteries are utilized to enhance the vitality thickness. Graphene-leading polymers and graphene-carbon nanotubes were additionally utilized in this application for their conductivity [90].

7.3. Optical applications

Polyamide-diminished graphene nanocomposites had been utilized for LED warm administration by Cho et al. The titanite coupling specialist utilized in this examination diminished the air voids present in decreased graphene sheets by responding with water particles. This expanded the heap exchange over the polymer and graphene as well as the warm conductivity of the composite. With high warm dissemination and better solidness, an LED light was hence made conceivable. A solitary layer of graphene is found to have a warm conductivity of 5300 W/(m·K), the warm conductivity for a PA/rGO had expanded by 53% in this work [91].

7.4. Graphene for composites under low-temperature conditions

Lately, graphene materials are of extraordinary consideration because of their ideal mechanical, electrical, and warm properties. Moreover, their extensive surface region as contrasted and other nano-basic materials make its standards as nano support for some polymer-based composites [92]. Figure 8 demonstrates the particular surface territory of various particles for building applications. Clearly, with a similar weight level of the particles, graphene and graphene oxide (GO) are smallest particles in the chart having moderately big surface region as contrasted and different particles. The utilization of GO, an oxidation type of graphene as fillers for polymer-based auxiliary individuals, has shown up in many building applications. GO is comprised of oxidative trash reinforced solidly to functionalized graphene sheets. It has a substantial surface zone (2630 m^2/g), high inherent portability (200,000 cm^2/V), high Young's modulus (~1.0 TPa), high warm conductivity (~5000 W/(m·K)), and high optical transmittance (~97.7%) [93]. It is typically arranged by the treatment of a graphite piece with anhydrous sulfuric corrosive, sodium nitrate, and potassium permanganate whose polar gatherings are presented onto the graphite's surface in this way, extending the interlayer dispersing of the graphene planes [94]. GO deals well with attributes and high concoction reactivity because of the nearness of the epoxide-, carboxyl-, carbonyl-, and hydroxyl-useful gatherings [95, 96].

7.5. Miscellaneous applications

Graphene-based paints include conductive ink, antistatic, electromagnetic-obstruction protecting, and gas hindrance. A large portion of graphite mining organizations including the new companies have customized fluid stage or thermally shed graphene in light of the fact that the generation innovation is straightforward and sensibly created.

8. CONCLUSION

From this survey, it can been seen that a couple of examiners consider reported that the age of bewildering graphene auxiliaries in a ground-breaking strategy and on a mass scale remain the bottlenecks that ought to be vanquished at the essential event to engage graphene's feasible applications. A couple of considered explorations propelled the way that artificially functionalizes the outside of graphene (therefore achieving a not too bad interfacial joint effort) would update its pertinence, especially inside the imperativeness and environmental sections. Thus, enhancing the major subtleties (for example, accomplishing a coherently drawn-out morphology) would be firmly persuading on its mechanical properties. Furthermore, the fortifying limit and, thus, their strippings are enhanced by defeating the mutilations and wrinkles in the platelets. Up until this point, biomedicine and other bio-based applications have the epic spotlight graphene related to research fields. Regardless, the purposes of restriction must be crossed considering the conventional estimations of graphene and its reinforcements.

The greater part of the carbon-based nanomaterial has the stunning enemy of bacterial action, with rGO being the most grounded. Thus, further obligations pinpointing the nanocarrier biocompatibility and security redesign along with measure and poisonous quality decay are of the utmost importance.

REFERENCES

[1] Mohan V. (2016). *Development of Functional Polymer-Graphene Nanocomposites* (Doctoral dissertation), ResearchSpace@ Auckland).

[2] Mohan V.B., Liu D., Jayaraman K., Stamm M. & Bhattacharyya D. (2016). Improvements in electronic structure and properties of graphene derivatives. *Advanced Materials Letters*, 7(6), 421–429.

[3] Mohan V.B., Brown R., Jayaraman K. & Bhattacharyya D. (2015). Characterisation of reduced graphene oxide: Effects of reduction variables on electrical conductivity. *Materials Science and Engineering: B*, 193, 49–60.

[4] Novoselo K.S., & Geim A.K. (2007). The rise of graphene. *Nature Materials*, 6(3), 183–191.

[5] Castro Neto A.H., Guinea F., Peres N.M.R., Novoselov K.S. & Geim A.K. (2009). The Electronic Properties of Graphene, *Reviews of Modern Physics*, 81, 109–162.

[6] Moghadam A.D., Omrani E., Menezes P.L. & Rohatgi P.K. (2015). Mechanical and tribological properties of self-lubricating metal matrix nanocomposites reinforced by carbon nanotubes (CNTs) and graphene–a review. *Composites Part B: Engineering*, 77, 402–420.

[7] Stoller M.D., Park S., Zhu Y., An J. & Ruoff R.S. (2008). Graphene-based ultracapacitors. *Nano Letters*, 8(10), 3498–3502.

[8] Kuilla T., Bhadra S., Yao D., Kim N.H., Bose S. & Lee J.H. (2010). Recent advances in graphene based polymer composites. *Progress in polymer science*, 35(11), 1350–1375.

[9] Geim A.K. (2009). Graphene: status and prospects. *Science*, 324(5934), 1530–1534.

[10] Ferrari A.C., Bonaccorso F., Fal'ko V., Novoselov K.S., Roche S., Bøggild P., Borini S., Koppens F.H., Palermo V., Pugno N. & Garrido J.A. (2015). Science and technology roadmap for graphene, related two-dimensional crystals, and hybrid systems. *Nanoscale*, 7(11), 4598–4810.

[11] Mohan V.B., Lau K.T., Hui D. & Bhattacharyya D. (2018). Graphene-based materials and their composites: a review on production, applications and product limitations. *Composites Part B: Engineering*, 142, 200–220.

[12] Hossain S.A., Hossen M. & Anower S. (2018). Estimation of damselfish biomass using an acoustic signal processing technique. *Journal of Ocean Technology*, 13(2), 91–109.

[13] Gadipelli S. & Guo Z.X. (2015). Graphene-based materials: Synthesis and gas sorption, storage and separation. *Progress in Materials Science*, 69, 1–60.

[14] Stankovich S., Dikin D.A., Dommett G.H., Kohlhaas K.M., Zimney E.J., Stach E.A., Piner R.D., Nguyen S.B.T. & Ruoff R.S. (2006). Graphene-based composite materials. *Nature*, 442(7100), 282–286.

[15] Novoselov K.S., Fal V.I., Colombo L., Gellert P.R., Schwab M.G. & Kim K. (2012). A roadmap for graphene. *Nature*, 490(7419), 192–200.

[16] Novoselov K.S., Geim A.K., Morozov S., Jiang D., Katsnelson M., Grigorieva I., Dubonos S.V. & Firsov A.A. (2005). Two-dimensional gas of massless Dirac fermions in graphene. *Nature*, 438(7065), 197–200.

[17] Dikin D.A., Stankovich S., Zimney E.J., Piner R.D., Dommett G.H., Evmenenko G., Nguyen S.B.T & Ruoff R.S. (2007). Preparation and characterization of graphene oxide paper. *Nature*, 448(7152), 457–460.

[18] Huang X., Qi, X., Boey F. & Zhang H. (2012). Graphene-based composites. *Chemical Society Reviews*, 41(2), 666–686.

[19] Hung P.Y., Lau K.T., Fox B., Hameed N., Lee J.H. & Hui D. (2018). Surface modification of carbon fibre using graphene-related materials for multifunctional composites. *Composites Part B: Engineering*, 133, 240–257.

[20] Layek R.K., Uddin M.E., Kim N.H., Lau A.K.T. & Lee J.H. (2017). Noncovalent functionalization of reduced graphene oxide with pluronic F127 and its nanocomposites with gum Arabic. *Composites Part B: Engineering*, 128, 155–163.

[21] Sun X., Liu X., Shen X., Wu Y., Wang Z. & Kim J.K. (2016). Graphene foam/carbon nanotube/poly (dimethyl siloxane) composites for exceptional microwave shielding. *Composites Part A: Applied Science and Manufacturing*, 85, 199–206.

[22] Bose S., Kim N.H., Kuila T., Lau K.T. & Lee J.H. (2011). Electrochemical performance of a graphene-polypyrrole nanocomposite as a supercapacitor electrode. *Nanotechnology*, 22(29), 295202.

[23] Bose S., Kuila T., Uddin M.E., Kim N.H., Lau A.K. & Lee J.H. (2010). In-situ synthesis and characterization of electrically conductive polypyrrole/graphene nanocomposites. *Polymer*, 51(25), 5921–5928.

[24] Hung P.Y., Lau K.T., Fox B., Hameed N., Lee J.H. & Hui D. (2018). Surface modification of carbon fibre using graphene-related materials for multifunctional composites. *Composites Part B: Engineering*, 133, 240–257.

[25] Ghosh S., Ghosh R., Guha P.K. & Bhattacharyya T.K. (2015). Humidity sensor based on high proton conductivity of graphene oxide. *IEEE Transactions on Nanotechnology*, 14(5), 931–937.

[26] Hossain S.A., Mallik A. & Arefin M. (2017). A Signal Processing Approach to Estimate Underwater Network Cardinalities with Lower Complexity. *Journal of Electrical and Computer Engineering Innovations*, 5(2), 131–138.

[27] Fang M., Wang K., Lu H., Yang Y. & Nutt S. (2009). Covalent polymer functionalization of graphene nanosheets and mechanical properties of composites. *Journal of Materials Chemistry*, 19(38), 7098–7105.

[28] Rosca I.D., Watari F., Uo M. & Akasaka T. (2005). Oxidation of multiwalled carbon nanotubes by nitric acid. *Carbon*, 43(15), 3124–3131.

[29] Istrate O.M., Paton K.R., Khan U., O'Neill A., Bell A.P. & Coleman J.N. (2014). Reinforcement in melt-processed polymer–graphene composites at extremely low graphene loading level. *Carbon*, 78, 243–249.

[30] Padmajan Sasikala S., Poulin P. & Aymonier C. (2016). Prospects of Supercritical Fluids in Realizing Graphene-Based Functional Materials. *Advanced Materials*, 28(14), 2663–2691.

[31] Zhang L.L., Zhou R., & Zhao X.S. (2010). Graphene-based materials as supercapacitor electrodes. *Journal of Materials Chemistry*, 20(29), 5983–5992.

[32] Chua C.K., & Pumera M. (2014). Chemical reduction of graphene oxide: a synthetic chemistry viewpoint. *Chemical Society Reviews*, 43(1), 291–312.

[33] Gao X., Jang J. & Nagase S. (2009). Hydrazine and thermal reduction of graphene oxide: reaction mechanisms, product structures, and reaction design. *The Journal of Physical Chemistry C*, 114(2), 832–842.

[34] Mohan V.B., Lau K.T., Hui D. & Bhattacharyya D. (2018). Graphene-based materials and their composites: a review on production, applications and product limitations. *Composites Part B: Engineering*, 142, 200–220.

[35] Liu H., Zhang L., Guo Y., Cheng C., Yang L., Jiang L., Yu G., Hu W., Liu Y. & Zhu D. (2013). Reduction of graphene oxide to highly conductive graphene by Lawesson's reagent and its electrical applications. *Journal of Materials Chemistry C*, 1(18), 3104–3109.

[36] Park S., An J., Potts J.R., Velamakanni A., Murali S. & Ruoff R.S. (2011). Hydrazine-reduction of graphite-and graphene oxide. *Carbon*, 49(9), 3019–3023.

[37] Hossain S.A., Ali M.F., Akif M.I., Islam R., Paul A.K. & Halder A. (2016). A determination process of the number and distance of sea objects using CHIRP signal in a three sensors based underwater network. In: *2016 3^{rd} International Conference on Electrical Engineering and Information Communication Technology (ICEEICT)*. IEEE, 1–6.

[38] Pei S., Zhao J., Du J., Ren W. & Cheng H.M. (2010). Direct reduction of graphene oxide films into highly conductive and flexible graphene films by hydrohalic acids. *Carbon*, 48(15), 4466–4474.

[39] Pham T.A., Kim J., Kim J.S. & Jeong Y.T. (2011). One-step reduction of graphene oxide with L-glutathione. *Colloids and Surfaces A: Physicochemical and Engineering Aspects,* 384(1–3), 543–548.

[40] Shin H.J., Kim K.K., Benayad A., Yoon S.M., Park H.K., Jung I.S., Jin M.I., Jeong H.-K., Kim J.M., Choi J.Y. & Lee Y.H. (2009). Efficient reduction of graphite oxide by sodium borohydride and its effect on electrical conductance. *Advanced Functional Materials*, 19(12), 1987–1992.

[41] Zhang J., Yang H., Shen G., Cheng P., Zhang J. & Guo S. (2010). Reduction of graphene oxide via L-ascorbic acid. *Chemical Communications*, 46(7), 1112–1114.

[42] Shen J., Hu Y., Shi M., Lu X., Qin C., Li C. & Ye M. (2009). Fast and facile preparation of graphene oxide and reduced graphene oxide nanoplatelets. *Chemistry of Materials*, 21(15), 3514–3520.

[43] Shen J., Hu Y., Shi M., Lu X., Qin C., Li C. & Ye M. (2009). Fast and facile preparation of graphene oxide and reduced graphene oxide nanoplatelets. *Chemistry of Materials*, 21(15), 3514–3520.

[44] Tang H., Ehlert G.J., Lin Y. & Sodano H.A. (2011). Highly efficient synthesis of graphene nanocomposites. *Nano Letters*, 12(1), 84–90.

[45] Gao X., Jang J. & Nagase S. (2009). Hydrazine and thermal reduction of graphene oxide: reaction mechanisms, product structures, and reaction design. *The Journal of Physical Chemistry C*, 114(2), 832–842.

[46] Wei Z., Wang D., Kim S., Kim S.Y., Hu Y., Yakes M.K., Laracuente A.R., Dai Z., Marder S.R., Berger C., King W.P., de Heer W.A., Sheehan P.E. & King W.P. (2010). Nanoscale tunable reduction of graphene oxide for graphene electronics. *Science*, 328(5984), 1373–1376.

[47] Chen W. & Yan L. (2010). Preparation of graphene by a low-temperature thermal reduction at atmosphere pressure. *Nanoscale*, 2(4), 559–563.

[48] Chen W., Yan L. & Bangal P.R. (2010). Preparation of graphene by the rapid and mild thermal reduction of graphene oxide induced by microwaves. *Carbon*, 48(4), 1146–1152.

[49] Wu T., Liu S., Li H., Wang L. & Sun X. (2011). Production of reduced graphene oxide by UV irradiation. *Journal of nanoscience and nanotechnology*, 11(11), 10078–10081.

[50] Lee G., Lee W., Nah S., Ji S., Hwang J.Y., Lee S.S., Parke S., Chae S.S. & Lee J.O. (2019). Solution-processable method for producing high-quality reduced graphene oxide displaying 'self-catalytic healing'. *Carbon*, 141, 774–781.

[51] Sadhukhan S., Ghosh T.K., Roy I., Rana D., Bhattacharyya A., Saha R., Chattopadhyay S., Khatua S., Acharya K. & Chattopadhyay D. (2019). Green synthesis of cadmium oxide decorated reduced graphene oxide nanocomposites and its electrical and antibacterial properties. *Materials Science and Engineering: C*, 99, 696–709.

[52] Tang H., Ehlert G.J., Lin Y., & Sodano H.A. (2011). Highly efficient synthesis of graphene nanocomposites. *Nano Letters*, 12(1), 84–90.

[53] McAllister M.J., Li J.L., Adamson D.H., Schniepp H.C., Abdala A.A., Liu J., Herrera-Alonso M., Milius D.L., Car R., Prud'homme R.K. & Aksay I.A. (2007). Single sheet functionalized graphene by oxidation and thermal expansion of graphite. *Chemistry of Materials*, 19(18), 4396–4404.

[54] Prusty K., Barik S. & Swain S.K. (2019). A Correlation between the Graphene Surface Area, Functional Groups, Defects, and Porosity on the Performance of the Nanocomposites. In: *Functionalized Graphene Nanocomposites and their Derivatives*, Elsevier, 265–283.

[55] Sun Y., Pan J., Zhang Z., Zhang K., Liang J., Wang W., Yuan Z., Hao Y., Wang B., Wang J. & Wu Y. (2019). Elastic Properties and Fracture Behaviors of Biaxially-Deformed, Polymorphic MoTe$_2$. *Nano Letters*, 19(2), 761–769.

[56] Chu L., Shi J. & Braun R. (2019). The equivalent Young's modulus prediction for vacancy defected graphene under shear stress. *Physica E: Low-dimensional Systems and Nanostructures*, 110, 115–122.

[57] Sari E., Uzek R. & Merkoçi A. (2019). Paper Based Photoluminescent Sensing Platform with Recognition Sites for Tributyltin. *ACS sensors*.

[58] Xu Y., Peng Y., You T., Yao L. Geng J., Dearn K.D. & Hu X. (2018). Nano-MoS$_2$ and Graphene Additives in Oil for Tribological Applications. In: *Nanotechnology in Oil and Gas Industries*, Springer, Cham, 151–191.

[59] Mohan V.B., Lau K.T., Hui D. & Bhattacharyya D. (2018). Graphene-based materials and their composites: a review on production, applications and product limitations. *Composites Part B: Engineering*, 142, 200–220.

[60] Luceño Sánchez J., Peña Capilla R. & Díez-Pascual A. (2018). High-Performance PEDOT: PSS/Hexamethylene Diisocyanate-Functionalized Graphene Oxide Nanocomposites: Preparation and Properties. *Polymers*, 10(10), 1169.

[61] Mohan V.B., Lau K.T., Hui D., & Bhattacharyya D. (2018). Graphene-based materials and their composites: a review on production, applications and product limitations. *Composites Part B: Engineering*, 142, 200–220.

[62] Sun X.Y., Liu H. & Ju S. (2019). Dependence of wrinkling geometric patterns on the chirality of monolayer graphene under shear deformation. *Physica E: Low-dimensional Systems and Nanostructures*, 105, 62–67.

[63] Farshid B., Lalwani G., Shir Mohammadi M., Srinivas Sankaran J., Patel S., Judex S., Simonsen J. & Sitharaman B. (2019). Two-dimensional graphene oxide reinforced porous biodegradable polymeric nanocomposites for bone tissue engineering. *Journal of Biomedical Materials Research Part A*, 14(3), 900–909.

[64] Guan L.Z., Zhao L., Wan Y.J. & Tang L.C. (2018). Three-dimensional graphene-based polymer nanocomposites: preparation, properties and applications. *Nanoscale*, 10(31), 14788–14811.

[65] Sakorikar T., Kavitha M.K., Tong S.W., Vayalamkuzhi P., Loh K.P. & Jaiswal M. (2018, May). Graphene: Polymer composites as moisture barrier and charge transport layer toward solar cell applications. In: *AIP Conference Proceedings*, Vol. 1953, No. 1, AIP Publishing, 100029.

[66] Young R.J., Kinloch I.A., Gong L. & Novoselov K.S. (2012). The mechanics of graphene nanocomposites: a review. *Composites Science and Technology*, 72(12), 1459–1476.

[67] Ren S., Cui M., Li Q., Li W., Pu J., Xue Q. & Wang L. (2019). Barrier mechanism of nitrogen-doped graphene against atomic oxygen irradiation. *Applied Surface Science*, 79, 669–678.

[68] Kumar A., Sharma K. & Dixit A.R. (2019). A review of the mechanical and thermal properties of graphene and its hybrid polymer nanocomposites for structural applications. *Journal of Materials Science*, 8, 1–35.

[69] Gavrilov S.N., Krivtsov A.M. & Tsvetkov D.V. (2019). Heat transfer in a one-dimensional harmonic crystal in a viscous environment subjected to an external heat supply. *Continuum Mechanics and Thermodynamics*, 31(1), 255–272.

[70] Moghaddasi Fereidani R. & Segal D. (2019). Phononic heat transport in molecular junctions: quantum effects and vibrational mismatch. *The Journal of Chemical Physics*, 150(2), 024105.

[71] Chowdhury S., Pan S., Balasubramanian R. & Das P. (2019). Three-Dimensional Graphene-Based Macroscopic Assemblies as Super-Absorbents for Oils and Organic Solvents. In: *A New Generation Material Graphene: Applications in Water Technology*, Springer, Cham, 43–68.

[72] Mallik A., Hossain S.A., Karim A.B. & Hasan S.M. (2019). Development of LOCAL-IP based Environmental Condition Monitoring using Wireless Sensor Network. *International Journal of Sensors, Wireless Communications and Control*, 9, 1–8

[73] Hajjar Z., Morad Rashidi A. & Ghozatloo A. (2014). Enhanced thermal conductivities of graphene oxide nanofluids. *International Communications in Heat and Mass Transfer*, 57, 128–131.

[74] Renteria J.D., Ramirez S., Malekpour H., Alonso B., Centeno A., Zurutuza A., Cocemasov A.I., Nika D.L. & Balandin A.A. (2015). Strongly anisotropic thermal conductivity of free-standing reduced graphene oxide films annealed at high temperature. *Advanced Functional Materials*, 25(29), 4664–4672.

[75] Wang F., Wang H. & Mao J. (2019). Aligned-graphene composites: a review. *Journal of Materials Science*, 54(1), 36–61.

[76] Tian J., Shi H., Hu H., Chen B., Bao Y. & Tang P. (2019). Implementation of Atomically Thick Graphene and Its Derivatives in Electromagnetic Absorbers. *Applied Sciences*, 9(3), 388.

[77] Del Giudice F., Cunning B.V., Ruoff R.S. & Shen A.Q. (2018). Filling the gap between transient and steady shear rheology of aqueous graphene oxide dispersions. *Rheologica Acta*, 57(4), 293–306.

[78] Shahzad F., Alhabeb M., Hatter C.B., Anasori B., Hong S.M., Koo C.M. & Gogotsi Y. (2016). Electromagnetic interference shielding with 2D transition metal carbides (MXenes). *Science*, 353(6304), 1137–1140.

[79] Henriques P.C., Borges I., Pinto A.M., Magalhaes F.D. & Gonçalves I.C. (2018). Fabrication and antimicrobial performance of surfaces integrating graphene-based materials. *Carbon*, 132, 709–732.

[80] Avijit M. & Hasan M. (2018). PV/T Systems for Renewable Energy Storage: A Review. *World Scientific News*, 96, 83–95.

[81] Chen F., Ying J., Wang Y., Du S., Liu Z. & Huang Q. (2016). Effects of graphene content on the microstructure and properties of copper matrix composites. *Carbon*, 96, 836–842.

[82] Tapasztó O., Tapasztó L., Lemmel H., Puchy V., Dusza J., Balázsi C. & Balázsi K. (2016). High orientation degree of graphene nanoplatelets in silicon nitride composites prepared by spark plasma sintering. *Ceramics International*, 42(1), 1002–1006.

[83] Karim A.B., Avro S.S. & Shahriar S. (2019). Prospect of Geothermal Energy Resources in Bangladesh. *International Journal of Renewable Energy Resources*, 8(2), 22–28.

[84] Wang X.D., Zhou J., Lao C.S., Song J.H., Xu N.S. & Wang Z.L. (2007). In situ field emission of density-controlled ZnO nanowire arrays. *Advanced Materials*, 19(12), 1627–1631.

[85] Zhong B., Dong H., Luo Y., Zhang D., Jia Z., Jia D. & Liu F. (2017). Simultaneous reduction and functionalization of graphene oxide via antioxidant for highly aging resistant and thermal conductive elastomer composites. *Composites Science and Technology*, 151, 156–163.

[86] Svidró J. & Diószegi A. (2018). New Possibilities in Thermal Analysis of Molding Materials. *Journal of Casting & Materials Engineering*, 2(4), 67–69.

[87] Fernández-Calvo A.I., Lizarralde I., Sal E., Rodriguez P., de Zabalegui E.O., Cia I. & Rios A. (2019). Grain-Size Prediction Model in Aluminum Castings Manufactured by Low-Pressure Technology. *Journal of Casting & Materials Engineering*, 2(4), 71–77.

[88] Mallik A., Arefin M.A. & Shahadat M.M.Z. (2018). Design and feasibility analysis of a low-cost water treatment plant for rural regions of Bangladesh. *AIMS Agriculture and Food*, 3(3), 181–204. Doi: 10.3934/agrfood.2018.3.181.

[89] Kaiser M.S. (2018). Effects of solution treatment on wear behaviour of Al-12Si-1Mg piston alloy containing trace Zr. *Journal of Casting & Materials Engineering*, 2(2), 30–37.

[90] Hossain S.A., Ali M. F., Akif M. I., Islam R., Paul A.K., & Halder A. (2016). A determination process of the number and distance of sea objects using CHIRP signal in a three sensors based underwater network. In: *Electrical Engineering and Information Communication Technology (ICEEICT), 2016 3rd International Conference on*, 1–6. IEEE, 2016.

[91] Nahian M.R., Zaman M.S., Islam M.N. & Rokunuzzaman M. (2018). Development of a Pressure Sensing Module and Flow Control System for a Prototype Pump Test Bed. *Indonesian Journal of Electronics and Instrumentation Systems*, 8(2), 155–166.

[92] Huang C., Fu S., Zhang Y., Lauke B., Li L. & Ye L. (2005). Cryogenic properties of SiO_2/epoxy nanocomposites. *Cryogenics*, 45(6), 450–454.

[93] Kim S., Young J.C., Hwi J.W., Qijun S., Sungjoo L., Moon S.K., Young J.S., Zhong L.W. & Jeong H.C. (2018). Piezotronic Graphene Barristor: Efficient and Interactive Modulation of Schottky Barrier. *Nano Energy*, 50, 598–605.

[94] Lim N., Tae J.Y., Jin T.K., Yusin P., Yogeenth K., Hyeonghun K., Woochul K., Byoung H.L. & Gun Y.J. (2018). Tunable graphene doping by modulating the nanopore geometry on a SiO_2/Si substrate. *RSC Advances*, 8(17), 9031–9037.

[95] Li Z., Wang R., Young R.J., Deng L., Yang F. & Hao L. (2013). Control of the functionality of graphene oxide for its application in epoxy nanocomposites. *Polymer*, 54(23), 6437–6446.

[96] Jacob G.J, Bandyopadhyay A., Bhowmick A.K. (2008). New generation layered nanocomposites derived from ethylene-co-vinyl acetate and naturally occurring graphite. *Journal of Applied Polymer Science*, 108(3), 1603–1616.